

Neuroinformatics

IN THIS ISSUE

The Impact of the NIH
Public Access Policy
on Literature Informatics

Statistical Criteria
in fMRI Studies
of Multisensory Integration

Comparison of Vector Space
Model Methodologies to
Reconcile Cross-Species
Neuroanatomical Concepts

Development of a Model for
Microphysiological Simulations

Editors

Giorgio A. Ascoli

Erik De Schutter

David N. Kennedy

Indexed and Abstracted in:
Medline/Pubmed/Index Medicus
Science Citation Index®

Original Article

Development of a Model for Microphysiological Simulations

Small Nodes of Ranvier From Peripheral Nerves of Mice Reconstructed by Electron Tomography

Gina E. Sosinsky^{1,*}, Thomas J. Deerinck¹, Rocco Greco¹, Casey H. Buitenhuis¹, Thomas M. Bartol² and Mark H. Ellisman^{1,*}

¹ National Center for Microscopy and Imaging Research, Department of Neurosciences and the Center for Research on Biological Systems, University of California, San Diego, CA² Computational Neurobiology Laboratory, Salk Institute, La Jolla, CA

Abstract

The node of Ranvier is a complex structure found along myelinated nerves of vertebrate animals. Specific membrane, cytoskeletal, junctional, extracellular matrix proteins and organelles interact to maintain and regulate associated ion movements between spaces in the nodal complex, potentially influencing response variation during repetitive activations or metabolic stress. Understanding and building high resolution three dimensional (3D) structures of the node of Ranvier, including localization of specific macromolecules, is crucial to a better understanding of the relationship between its structure and function and the macromolecular basis for impaired conduction in disease. Using serial section electron tomographic meth-

ods, we have constructed accurate 3D models of the nodal complex from mouse spinal roots with resolution better than 7.5 nm. These reconstructed volumes contain 75–80% of the thickness of the nodal region. We also directly imaged the glial axonal junctions that serve to anchor the terminal loops of the myelin lamellae to the axolemma. We created a model of an intact node of Ranvier by truncating the volume at its midpoint in Z, duplicating the remaining volume and then merging the new half volume with mirror symmetry about the Z-axis. We added to this model the distribution and number of Na⁺ channels on this reconstruction using tools associated with the MCell simulation program environment. The model created provides accurate structural descriptions of the membrane compartments, external spaces, and formed

*Authors to whom all correspondence and reprint requests should be addressed.
E-Mail: gsosinsky@ucsd.edu; mark@ncmir.ucsd.edu

structures enabling more realistic simulations of the role of the node in modulation of impulse propagation than have been conducted on myelinated nerve previously.

Abbreviations: PNS=peripheral nervous system, CNS=central nervous system, HPF=high pressure freezing, EMT=electron microscopic tomography

DOI: 10.1385/NI:03:02:133

Index Entries: Myelinated axons; peripheral nerve structure; saltatory conduction; ionic transmission; three-dimensional reconstruction; electron microscopy; cell-cell junctions, axonal-glia interactions; high pressure freezing.

Introduction

The nodes of Ranvier allow amplification and regeneration of action potentials and are relatively recent evolutionary adaptations found in most vertebrates. The first to observe these structures was Louis-Antoine Ranvier who in 1878 described the basic anatomical features as periodic constrictions of nerve fibers. These specialized and complex structures reflect the functions these sites serve in the saltatory propagation of large ionic currents and the regeneration of resting membrane potentials. Saltatory conduction allows more rapid propagation of action potentials without large increases in axonal diameter and limits large ionic fluxes to very localized domains of the nerve axons. Numerous studies (Carley and Raymond, 1987; Endres et al., 1986; Halter and Clark, 1993; Lev-Ram and Ellisman, 1995; Lev-Ram and Grinvald, 1986; Lev-Ram and Grinvald, 1987; Murray and Steck, 1984; Wurtz and Ellisman, 1986) support the hypothesis that the axon/myelin/glia cell ensemble or "nodal complex" operates in an integrated manner during conduction of the nerve impulse. Pathological conditions in peripheral neuropathies occur due to abnormalities in node of Ranvier constituent proteins (Bergoffen et al., 1993; Griffin et al., 1996; Sima, 1993), axonal ischemic injury (Waxman et al., 1992) and trauma (Maxwell et al., 1991). Regeneration of damaged peripheral nerve axons also occurs at the nodes of Ranvier (Fawcett and Keynes, 1990). The

nodes of Ranvier represent an excellent example of structural specialization and organization in that they contain highly regulated, recognizable membrane domains containing specific integral proteins, and distinct morphological structures connected to more than one cell type.

New methods for ultrastructural analysis are available including methods for direct localization of macromolecules that have expanded our understanding of the structure of the nodal region. Concomitantly, our understanding of the structure/function relationship of the node of Ranvier has evolved from a simple site for concentration of ion channels, to one based on expanding knowledge of the node as an extremely complex and dynamic structure with multiple ionic and metabolic compartments (see Fig. 1). Within the nodal complex there are also junctions of nearly every class (tight, gap, adherens, septate-like) including several formed between adjoining processes of the same cells. In particular, the paranodal regions of nodes of Ranvier contain gap junctions (made up primarily of connexin32), the septate-like axoglial junctions (containing the proteins, caspr/paranodin and contactin, (Boyle et al., 2001; Poliak et al., 2001; Tait et al., 2000), and tight junctions (containing ZO1 and other tight junction proteins). Adherens junctions containing E-cadherin have cytoskeletal proteins such as F-actin, spectrin and beta-catenin associated with them (Fannon et al., 1995; Trapp et al., 1989). These adherens junctions connect the myelinating glia to the axon

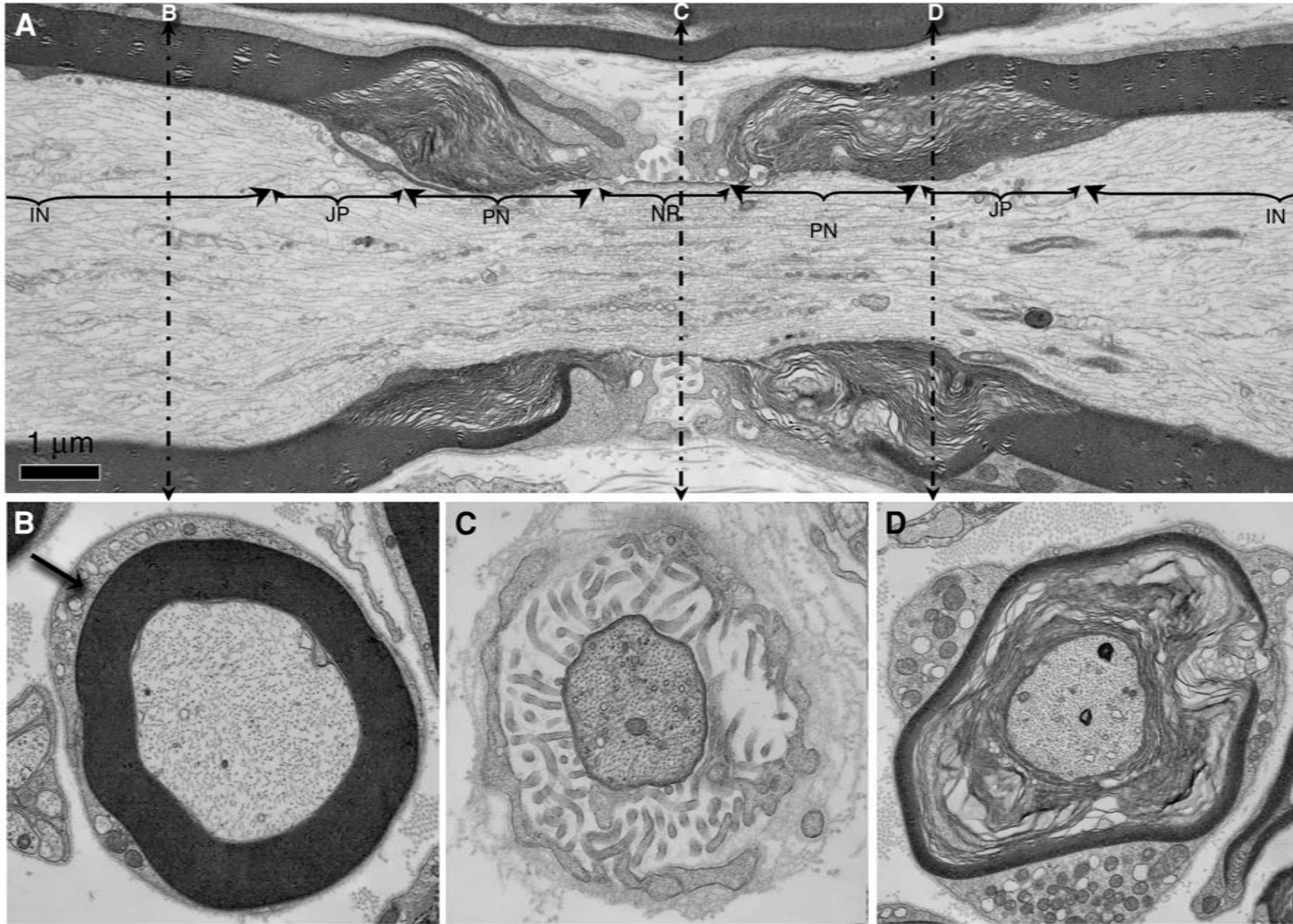


Fig. 1. Continued.

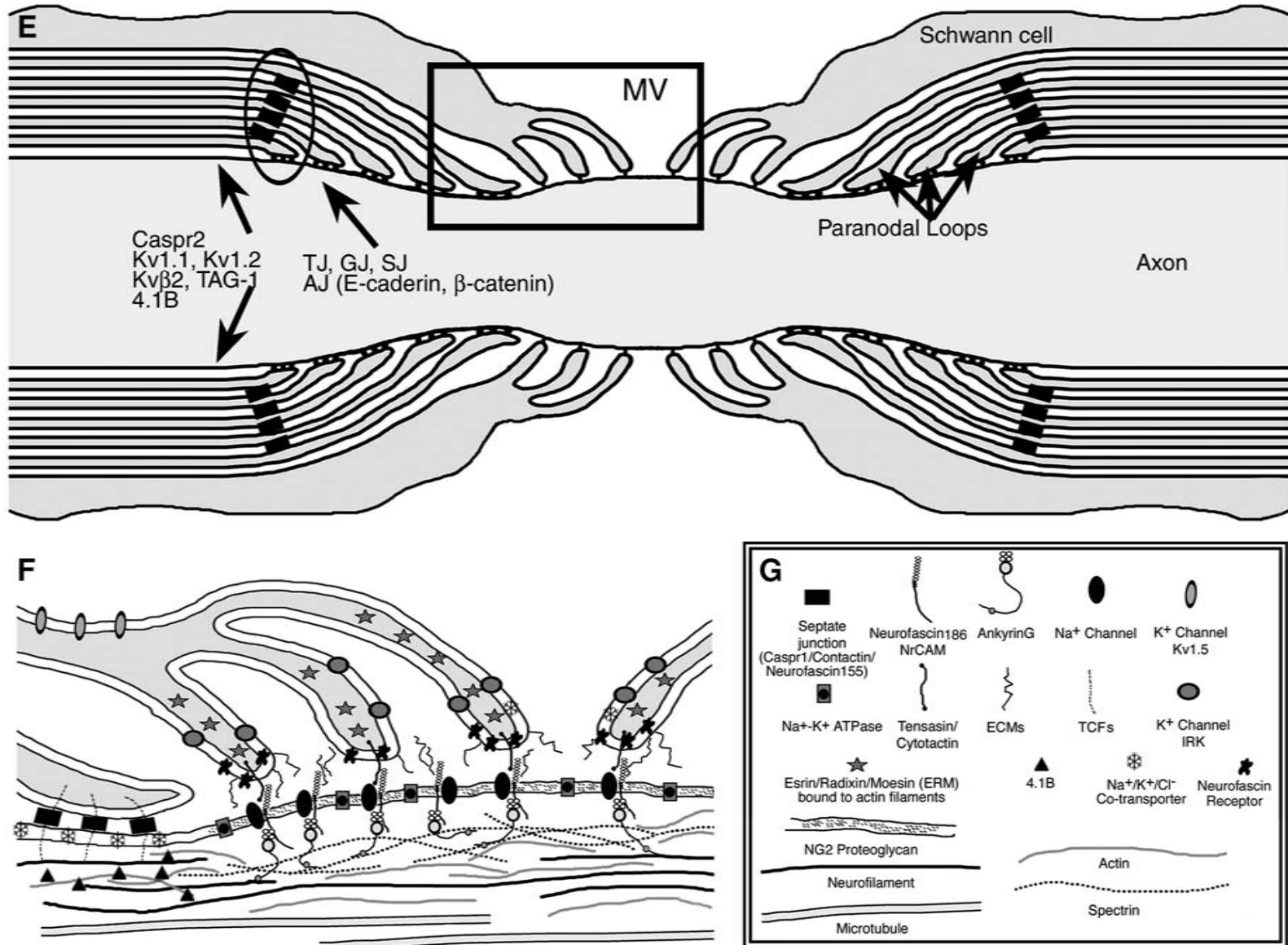


Fig. 1. Continued.

and myelin lateral loops to one another. Tight junctions seal the periaxonal space of the paranodal region from the intra-myelin space. In a system where fluctuations in state and dimensions of compartments have been demonstrated by physiological and microanatomical studies, one can safely predict the existence of elaborate mechanisms to manage and maintain the precise replacement of membrane molecular machinery and to modulate the dynamic properties of the overall complex.

In the early 1990s, (Ichimura and Ellisman, 1991) published a three-dimensional (3D) model of the fine structure of the nodal complex based on conventional and high voltage electron microscopy of thin and semi-thick sections and freeze fracture and deep-etching. The model resulting from these structural studies contained transcellular structures across the nodal gap and traversing the paranodal glial-axonal junction. Both extracellular gap-crossing filaments and membrane-cytoskeletal linkers in the nodal axoplasm are joined to prominent membrane particles of the nodal axolemma. At the paranodal glial-axonal junction, the anchoring sites of other membrane-cytoskeleton linkers are linear arrays of 16 nm particles. Cytoplasmic filaments and extracellular filaments or bridge structures are involved in the membrane-cytoskeletal inter-

action at the node and paranode. Some of these membrane particles are Na⁺ channels that play a role in ionic conductance that occur at this site (Ellisman et al., 1982) and paranodal-axonal junctional proteins such as Caspr play a role in maintenance of the segregation of these channels in the nodal membrane (Rios et al., 2003).

Here we present 3D representations of the node of Ranvier from young mice as obtained using serial section electron microscopic tomography (EMT). The use of EMT has been critical in recent years to understanding the structure and organization of large scale organelles such as mitochondria (Mannella et al., 1994; Nicastro et al., 2000; Perkins et al., 1997a), the Golgi apparatus (Ladinsky et al., 1994; Marsh et al., 2001), actin networks in the leading edge of cells (Medalia et al., 2002), septal pores (Martin et al., 2001) as well as deciphering tissue level organization of structures in the nervous system (Harlow et al., 2001; Lenzi et al., 1999; Martone et al., 1999; Shoop et al., 2002). Because of the size and complexity of the node of Ranvier, the 3D structure cannot be inscribed in a single thick (0.5–1 μm) section that is typically used with standard 300–400 keV electron microscopes. Instead, for this work, we chose to use three 0.5 μm sections that make up approx 75–80% of the width of small nodes and paranodes and

Fig. 1. Organization of the peripheral node of Ranvier. (A) Electron micrograph of a thin section through a node of Ranvier from a longitudinal section of adult rat ventral spinal root with the nodal (NR), paranodal (PN) and internodal areas (IN) marked. Cross sections through various regions of axons from adult rat ventral spinal roots are shown in **(B–D)**. **(B)** Section through the internodal region of an axon. The outer layer of Schwann cell cytoplasm is reduced to narrow channels, or canaliculi (arrow), that run continuously from the cell body to the nodal region. **(C)** Section through the midpoint of the nodal membrane. Numerous Schwann cell microvilli can be seen surrounding and closely apposing the axonal nodal membrane. The basal lamina covers the entire nodal region. **(D)** Section through the paranodal region of an axon. The dramatic changes in axon diameter and axoplasmic density can be seen in each region. **(E)** Schematized version of the membrane systems shown in **(A)**. Junctional structures are also indicated. **(F)** Schematic diagram of a portion of a node of Ranvier illustrate the complex membrane-cytoskeletal interactions observed at the node of Ranvier. The cytoskeletal filaments include microtubules, neurofilaments, glial filaments and finer filaments of various sizes. Subsets of these filaments anchor to the cytoplasmic end of transmembrane structures or proteins. **(G)** Key to the proteins schematically shown in **(F)**.

merge the 7three volumes into one. This has the benefit of having better resolution in the z direction as well as encompassing the majority of the structure. In this structure, subcellular components such as adherens junctions, neurofilaments, microtubules and membrane systems are obvious. Membrane components are segmented to obtain continuous compartmentalized structures. This approach can be used as the starting basis for creating models to study ionic transmission and, in higher resolution tomograms, to identify the septate-like junction macromolecular complex in a beginning step to directly visualize the protein arrangements. Accurately constructed and detailed models are important tools for the development of microphysiological simulation experiments (Esquenazi et al., 2001; Shoop et al., 2002).

Materials and Methods

Three- or seven-day-old mice were anesthetized and perfused with a balanced salt solution (135 mM NaCl, 14 mM NaHCO₃, 1.2 mM Na₂HPO₄, 5 mM KCl, 2 mM CaCl₂ and 1 mM MgCl₂) at 37°C. This was followed by perfusion with a solution of 2% glutaraldehyde and 2% formaldehyde in 0.15 M sodium cacodylate (pH 7.4) for 5 min. For optimal structural preservation, the formaldehyde was made fresh from paraformaldehyde. Dorsal and ventral spinal roots as well as sciatic and saphenous nerves were removed and fixed for an additional 1 h on ice in the glutaraldehyde/formaldehyde fixative. Tissue was postfixed with 2% OsO₄ in cacodylate buffer for 1 h, rinsed in double distilled water, dehydrated in graded ethanol and embedded in Durcupan ACM resin (Electron Microscopy Science Inc.). Thin (100 nm) sections and semi-thin (0.5–2 μm) sections were cut using a diamond knife (Diatome) and an Ultracut E ultramicrotome (Leica) and mounted on uncoated copper grids. Thin sections were imaged at 80 keV using a 100CX or 2000FX

electron microscope (JEOL) and semi-thin sections were imaged at 300–400 KeV using a 4000EX intermediate voltage electron microscope (JEOL).

High Pressure Freezing (HPF) and Preparation of Freeze-Substituted Material

We used the Bal-Tec HPF010 located in the Electron Microscopy lab at UC Berkeley for HPF for these experiments and used the HPF/FS procedure described in (McDonald, 1999). The nerves were gently cut into small segments in order to fit into Bal-Tec specimen hats and filled with freshly made yeast paste. The top specimen carrier was added to the specimen carrier, closed and frozen in the HPF machine at approx 123°K and approx 2100 bar. The specimens were transferred to the Leica Automatic Freeze Substitution Unit (AFS) in freeze substitution cocktail (2% osmium, 0.1% uranyl acetate in acetone) maintained at –155°C and warmed up to –90°C at 5°/h. The entire process was maintained at –90°C for 72 h with intermittent agitation. The specimen was then warmed to +20° C at 10°C/h. The samples were subsequently rinsed with three incubations of pure acetone for 10 min with gentle rocking. Samples were then removed from aluminum sample holders and infiltrated with mixtures of 3:1 acetone:Epon for 2 h, then changed to 1:1 acetone:Epon mixture for 4 h, then incubated in 1:3 acetone:Epon for 8 h. Finally, the preserved nerve tissue was put into in pure Epon overnight and embedded in thin layers on slides and polymerized for 48 h at 60°C. Sections were post-stained with uranyl acetate and Saito lead solution (lead citrate, lead nitrate, lead acetate).

EMT Data Acquisition

Sections of 0.25 or 0.5 μm in thickness were cut. Sections were post-stained with uranyl acetate and lead citrate. Colloidal gold particles

were applied to the top of the mounted sections and serve as markers for fiducial alignment during the image reconstruction process. Grids were examined at 400 kV using a specially designed JEOL 4000 IVEM (Fan et al., 1996). Tilt series consisting of 61 images (-60° to 60° at 2° tilt increments) were collected at 20–25,000x magnifications. In the tomograms presented in Figs. 2 and 3, tilt series number 3 contained only angles -58° to 38° due to obstruction at high tilt from the grid bar. The magnification was chosen in order to fit the entire width of the nodal region (node plus two surrounding paranodes). For imaging at higher resolution, the magnification was chosen as 40–60,000x to allow for a suitable area to be imaged at pixel sizes small enough to resolve macromolecular components.

Image Processing and 3D Reconstruction

Images recorded on film were scanned at approx 50–70 μm pixel size with a Photometrics camera using a 1k x 1k Thomson CCD with 19 μm pixels and 14 bit dynamic range. The tilt images were aligned by use of fiducial marks common to the set of images. The alignment was checked and markers repositioned. Optimal alignments were achieved via a least-square fitting program and images were re-calculated with the rotation and translation vectors obtained from the least square fitting (Perkins et al., 1997). For the data set shown in Fig. 7, each single tilt tomogram was computed using the IMOD package (URL <http://bio3d.colorado.edu/imod/index.html>). The IMOD package (Kremer et al., 1996) contains distortion correction algorithms that become more important in higher magnification/higher resolution tomograms such as the reconstruction of the glial-axonal junctions. A tomographic volume was created using standard R-weight back projection algorithms. The 3D reconstructions were viewed and analyzed with the program ANALYZE (URL <http://www.mayo.edu/bir/Software/Analyze/Analyze.html>).

Merging of Serial Volumes

Serial section electron tomographic reconstruction was accomplished using the method originally developed by this laboratory and described as a method for reconstruction of entire cells and subcellular complexes in (Soto et al., 1994). In order to match up key features at the top and bottom slices of the tomograms, the serial volumes were corrected for the tilt, curvature or unevenness of the section using the oblique option in ANALYZE. Then, the slices in each tomogram were output as individual files in order to determine the order of the tomograms. Key features such as paranodal cisternae and mitochondria in the top and bottom slices determine the order of the individual volumes. The rotation and translation vectors were determined for aligning each volume with respect to the others starting with the center section as a reference and working outwards. To find rotation and translation vectors, sections from the top and bottom of two volumes were either manually aligned with the program SLIME (Steve Lamont, NCMIR) or automatic single particle alignment procedures were used using SUPRIM (Frank, 1989). The vector information (angle of rotation, translation offsets) was applied to all individual sections in the volumes. The slices in each series were edited to eliminate empty and incomplete sections at the top and bottom from either over-computation of sections or padding during the oblique correction. Aligned individual sections were recombined into an ANALYZE 3D volume. The volume was then rotated in ANALYZE so that the axonal axis ran horizontal and the volume was cropped in preparation for segmentation.

Double Tilt EMT

The limited tilt range of data collection of EMT produces a wedge of missing data that causes distortion in the reconstructions and

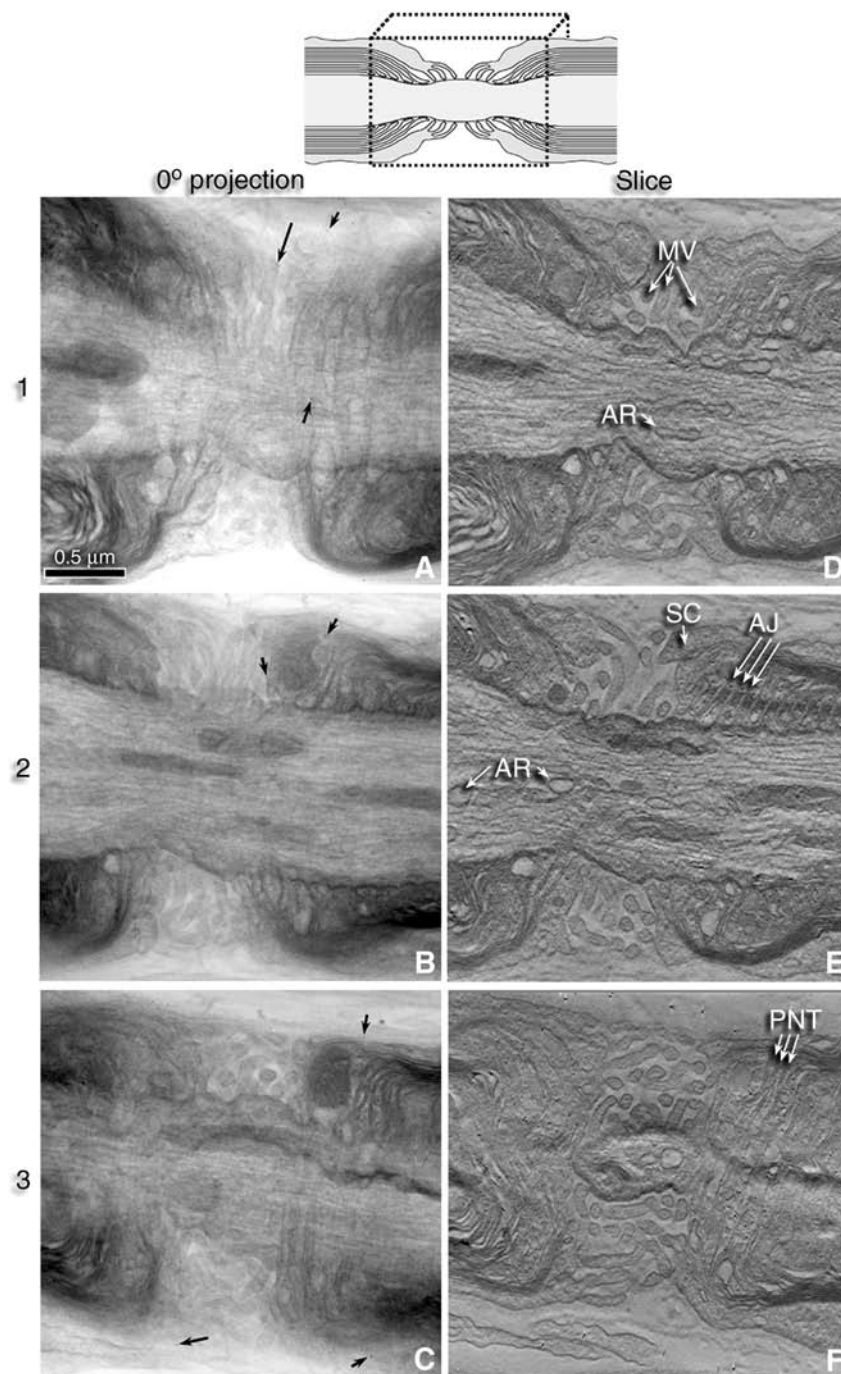


Fig. 2. Projections and slices from well-preserved material from spinal roots prepared by conventional methods. Top: box on node of Ranvier schematic indicates 3D location of tomogram. We reconstructed tomograms from tilt series of each of these three 0.5- μm sections at a magnification of 25,000x. **(A, B, C)** The 0° tilt from each of the tilt series. The black arrows point to examples of fiducial gold beads. **(D, E, F)** Sample slices from the three individual tomographic slabs, are presented. These thin computed slices are approx 50Å thick. Abbreviations for some larger nodal components: **AR** = axoplasmic reticulum, **SC** = Schwann cell body, **AJ** = adherens junction, **PNT** = paranodal loop terminations, **MV** = microvilli.

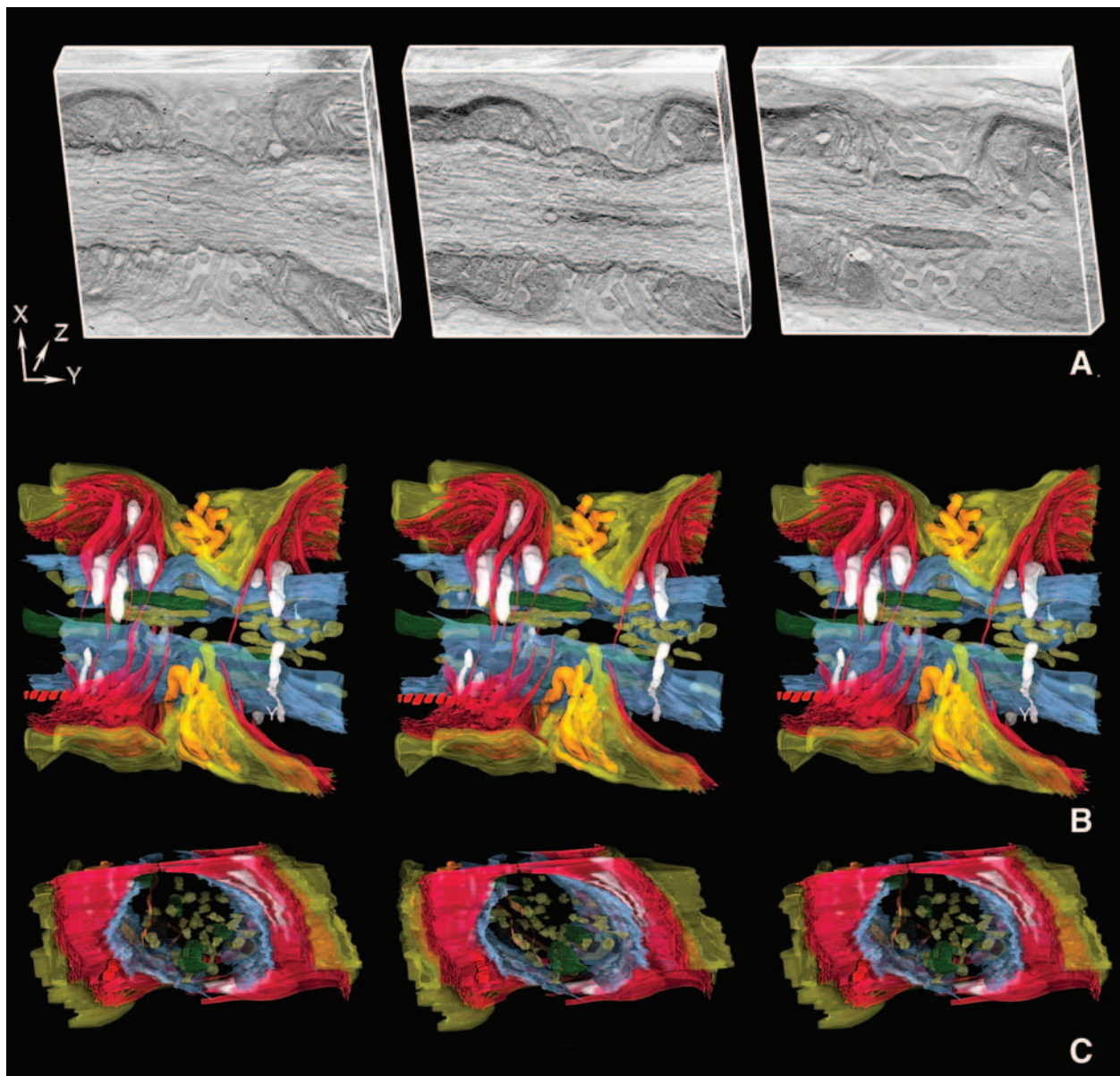


Fig. 3. Surface shaded representations of the components in the node of Ranvier complex. **(A)** The three volumes (shown here in cube representations) were aligned and merged into a single volume to examine the connectivity and relationship of key structural complexes. **(B, C)** Two orthogonal views (parallel and perpendicular to the axonal axis) orientations are shown in stereo. Structural elements were traced throughout the entire 1.2 μm . Key to feature and color-coding: Outer Schwann cell membrane = yellow; compact myelin and paranodal loops = magenta; microvilli = orange; adherens junctions = red; paranodal cisternae = white; microtubules = dark red; sub-surface axonal cisternae = green; axonal endoplasmic reticulum = light brown; axonal membrane = transparent blue. Note: only about 50% of the microvilli, two microtubules, less than 50% of the SER are represented here for ease of viewing and the paranodal loops were traced as unconnected. Stereo images are presented as “cross-eyed” (left two images) and “wall-eyed” (right two images). To view stereo “cross-eyed”, hold your finger 4–5 inches in front of your nose and then focus on your finger. In the distance the two images become one stereo image, with the separate images still visible on either side. Slowly focus on the center

anisotropic resolution, typically in the axis oriented perpendicular to the tilt axis (Mastronarde, 1997; Penczek et al., 1995). To reduce the missing wedge to a pyramid, two complete data sets (61 or 121 images) were recorded in orthogonal directions and the volumes were merged. For a specimen that contains a long axis (such as the axonal axis of the node of Ranvier), the first data set was recorded in the short axis perpendicular to the axonal axis of the node. The grid was then rotated either using the rotate-tilt stage of the JEOL 4000 or removed from the single tilt holder and manually rotated. IMOD utilities were used for the merging of orthogonal tilt volumes. Merging of volumes was based on least square refinement of common fiducial markers and with general 3D linear transformations that correct for distortions between the two tomograms.

Graphical Representations of Node Structure and Organization

Features (membrane regions, organelles and cytoskeletal elements) were traced using XVOXTRACE and rendered using the SYNU 3D graphics package. Graphical representations combining volume and surface rendering were computed using the program AMIRA (TGS Inc., San Diego, CA). Based on the merged volumes from the three serial sections, the midline of the node was determined by measuring the largest diameter in the cross-section ($x-z$ plane) of the nodal region. Using ANALYZE, the volume was cropped to approximate one complete half of the node of Ranvier. The vol-

ume was duplicated and the duplicate was flipped about the Z -axis to mirror its partner. The two symmetry related subvolumes were appended to one another. The ANALYZE volume was then imported into Amira and the axon was masked using a tetrahedral grid as a marker for exterior and interior space. Volume texturing and rendering were done using Amira's maximum intensity volume texturing tool. XVOXTRACE (Soto et al., 1994) was used to segment the axonal membrane in the volumes and the resulting surface was converted to IBM Open Visualization Data Explorer format for import into DReAMM (<http://www.mcell.psc.edu/DReAMM/>). DReAMM was used to mark the nodal region of the axonal membrane so that MCell could differentially distribute model ion channels by membrane region. The resulting model was rendered using DReAMM.

Deposition of the Tomographic Data Into the Cell-Centered Database

All of the reconstructions described in this report have been deposited in the Cell-Centered Database (<http://www.ccdb.ucsd.edu/CCDB>), a web-accessible database for 3D reconstructions from light and electron microscopy (Martone et al., 2002, 2003). The Cell Centered Database (CCDB) makes available the raw data, i.e., tilt images, tomographic volumes, segmentations and animations for viewing and download. Access to the CCDB requires an account which is available free of charge. A unique record ID that is supplied in the results section identifies each of the tomo-

image without re-converging the eyes. The center image becomes sharp and looks three-dimensional. To view stereo "walled-eyed", hold the stereo pair at a comfortable, viewing distance. The stereo-pair should be approximately in the center of your visual field and evenly illuminated. Looking "through" the paper, look to the distance. A third image will appear between the left and right pictures. Without converging the eyes, slowly focus on the third, center image, which should look three-dimensional. This description was adapted from http://www.edge-3d.com/how_to.htm. Stereo glasses for viewing wall-eyed stereo are available from electron microscopic supply companies such as Ted Pella, Inc. (Redding, CA).

graphic volumes. Entering this record ID in the "Record ID" field in the query form will retrieve the data for this reconstruction. Entering the Project ID can access the entire set of reconstructions reported here: P1136 in the "Project ID" field in the query form.

Results

Overview of Node of Ranvier Fine Structure

The node of Ranvier is an elegant and complex structure that has been studied extensively by light and electron microscopy (for the most recent comprehensive review see (Salzer, 2003). Fig. 1 provides an overview and summary of the present information based on the published literature about the node of Ranvier, morphological features and known protein constituents. Myelinated axons containing both the neuron and one more glial cells consist of four domains: the *nodal* region, the *paranodal* region, the *juxtaparanodal* region, and the *internode* (Fig. 1 A–E). The glial cells are Schwann cells in the peripheral nervous system and oligodendrocytes and astrocytes in the central nervous system) The thin section appearance of each of these different regions is shown in Fig. 1 A–D. The axonal component of the nodal region is defined as the space between the most superficial lateral loops of the adjacent myelinating glia and is the site of the high density of voltage dependent sodium channels (Ellisman and Levinson, 1982). The nodal membrane or nodal "gap" occupies about 1–2 μm of length along the axon and in peripheral nerves (*PNS*) the space above this region of the axolemma is overlaid by numerous Schwann cell microvilli. These microvilli are absent in central nervous system (*CNS*) nodes, where oligodendrocytes are the myelinating cell type, however, sheet or finger-like processes of adjacent astrocytes are found in very close apposition. At the paranode, the myelin lamellae open up to form cytoplasmic pockets, or as they appear in thin sections, "lateral loops",

which are part of a continuous helical structure providing cytoplasmic continuity from the innermost to the outermost layers of the myelin sheath through the cytoplasmic channel formed by the loop. Just beyond the terminal loops of the paranode lies the juxtaparanode followed by the internodal region. The dense wrapping of the myelin membrane at internodal regions ensures that the myelinating cell cytoplasm is reduced to small channels and that these channels run continuous down the length of each fiber from node to node. Diameters of cross-sections through the nerve are smallest in the paranode (Fig. 1D), slightly wider in the nodal regions (Fig. 1C), greatest in the internode (Fig. 1C) and irregular in the juxtaparanode.

Equally important in our understanding of ionic transmission is information on the precise distribution and density of molecules in the nodal complex. Figs. 1E–G are schematics of a *PNS* nerve detailing known molecular localizations and how these relate to morphological features within the nodal region. The locations of these molecules were obtained from previously published immunolocalizations (for example, neurofascin155 and neurofascin186 (Tait et al., 2000); E-cadherin (Fannon et al., 1995), periaxin (Gillespie et al., 1994; Scherer et al., 1995), caspr1/paranodin (Bhat et al., 2001), caspr2 (Poliak et al., 2001), contactin (Boyle et al., 2001), $\text{Na}^+/\text{K}^+/\text{Cl}^-$ cotransporter (Alvarez-Leefmans et al., 2001), NG2 proteoglycan (Martin et al., 2001), ankyrin_G (Lambert et al., 1997), ezrin/radixin/moesin (Melendez-Vasquez et al., 2001; Scherer et al., 2001) and demonstrates how various parts of the axonal and Schwann cell membranes are highly polarized and organized. The images, diagrams and drawings in Fig. 1 collated from information in the literature are presented as a framework for interpretation of the tomographic structures presented here and to show what molecular components would need to be included in microphysiological simulations.

3D Reconstructions of Conventional Preparations

We began this work by carrying out serial electron tomographic reconstruction and analysis of conventionally fixed specimens of peripheral nerves. We used P7 mice because their nodes of Ranvier have the same basic organization of nodes found in small fibers of adult nodes, but, with fewer layers of myelin, they manifest a more simplified paranodal apparatus in which all myelin segments attach to the paranode. As myelin thickens with more layers being added, paranodal terminations are not all attached to the paranodal axolemma, and form a specialized structure called the spiny bracelet of Nageotte (Berthold, 1996; Berthold et al., 1983). Since the early nodes of Ranvier of rats and mice are similar to those of small adult fibers we used these for the present study. This decision was based on the rationale that improved quality of preservation can be obtained from young myelinated fibers and also that in immature animals the spacing is shorter between nodes—making them more frequently encountered in sections examined in the electron microscope. Consequently, we chose the thinly myelinated fibers of young animals as a starting point for this effort to develop a procedure to construct models of nodes for microphysiological simulations. Three tilt series were collected that contained most of the node of Ranvier. We also examined a fourth serial section but could not record a tilt series because we could not correlate the nerve recorded in the previous three sections with any on the fourth section. Shown in Fig. 2A–C are the 0° tilt from each of the 0.5 μm sections. The three sections contain almost 75–80% thickness of a single node of Ranvier. The three individual tomographic “slabs” or volumes containing portions of this node were merged into a single volume approx 1.2 μm thick (CCDB Record ID: con_node). Single slices are shown in Fig. 2D–F. Accessing the data, volume and segmentations requires an

account in the CCDB that can be obtained free of charge at <http://www.ccdb.ucsd.edu/CCDB>). In the original micrographs, the structures appear fuzzy and indistinct due to the large overlap of material in the section, however, the subcellular structures, such as neurofilaments, adherens junctions, microvilli extensions, membranes and mitochondria, in the individual slices are crisp and well-defined. Of note in this particular reconstruction is the band of adherens junctions that can be expected to serve to anchor the paranodal myelin loops together (*see* central slice in Fig. 2E). The three volumes are illustrated in cube representations in Fig. 3A as one method for conveying their three dimensionality.

In order to assess the continuity of the structures in 3D, we used the program Xvoxtrace (Perkins et al., 1997b) to segment the merged volumes. We found that we could resolve many of the components of paranodal glial-axonal junction structures, indicating a resolution of better than 10 nm even at the relatively low magnification required to reconstruct an entire node by serial section EMT. Also remarkable was the ease with which we could follow the glial and axonal components of the paranodal cisternal and cytoskeletal systems. Following these components based on serial thin sections would be difficult to do with conventional methodologies as they are thin tubular anastomotic structures whose cross sectional diameters (~20 nm) are less than the thickness of the thinnest of ultra thin sections (~50 nm). Of interest for defining cellular compartments were not only the axonal membrane, Schwann cell membrane and uncompacted and compacted myelin membranes, but also the smooth endoplasmic reticulum (SER) systems of the paranodal loops and subparanodal axoplasm, microvilli of Schwann cells surrounding the nodal region and mitochondria in both the axonal and paranodal areas. Stereo pairs of two orthogonal views (parallel and perpendicular to the axonal axis and presented as either

cross-eyed or wall-eyed views) of the segmented volume are shown in Fig. 3B, C. Long elements such as axonal microtubules, neurofilaments, mitochondria and axonal endoplasmic reticulum follow the long axis of the nerve while elements of the paranode and Schwann cells such as the microvilli and paranodal cisternae are oriented on a axis perpendicular to the axon.

3D Reconstructions of sHPF and Freeze-Substituted Preparations

In order to evaluate the effects of various steps in preparation of material for EM such as fixation, osmification and dehydration on the supramolecular structure of the node, we prepared specimens using high pressure freezing and freeze substitution. Under optimal conditions, ultra-rapid freezing in combination with freeze substitution has proven to be superior to conventional fixation (Dahl and Staehelin, 1989; McDonald, 1999; Moor, 1987; Shimoni and Muller, 1998). For this study, aldehyde fixation was necessary in order to minimize structural damage during the time the spinal root nerves were surgically removed from the mice and transferred to the high pressure freezer. While conventionally fixed nerve is adequate in preserving nodal ultrastructure, HPF and freeze substitution reduce shrinkage artifacts due to dehydration and so more accurately reflect the native dimensions of structures (compare tomographic slices in Figs. 2 and 4).

A serial section tomographic reconstruction from three serial sections of a nodal region from 3-d-old mice was performed in a manner similar to that used for the conventional preparations as described above (Fig. 4: CCDB record ID: HPF_node). An annotated animation through the entire volume can be viewed without an account from the CCDB website at <https://ccdb.ucsd.edu/CCDB/animationprofile.htm> and clicking on the link to HPF-node. Again, 61 image tilt series from three 0.5- μ m sections were collected, reconstructed and merged.

Characteristics of good cell ultrastructure include dense, uniform cytoskeletal material and preservation of internal membrane organelles such as endoplasmic reticulum, Golgi apparatus and mitochondria. In these slices from tomograms computed from conventionally prepared spinal root nerves and from the HPF spinal root nerves, the myelin is much less distorted and swollen, all cell membranes appear linear as opposed to wavy and the cell cytoplasm contains more granular material than with conventionally prepared samples (*see* Fig. 4). These gross morphological features are just three indications of improved cellular preservation. In addition, cross-sections through microtubules in the paranodal loops (Fig. 4D) indicate better preservation of fine cytoskeletal elements within these compartments. As a result, this reconstruction was chosen for further use in developing functional models for programs that simulate ionic transmission.

Segmentation of this serial section tomographic reconstruction from three sections of a nodal region is shown in Fig. 5. In these graphical representations, the paranodal loops form a more symmetric and fluid arrangement than those in Fig. 3. The surface renderings (Fig. 5A,B) demonstrate the close apposition of the loops on the axonal membrane at the sites of the septate-like junctions. The density of material within the axonal compartment is illustrated in the volume rendering of the axonal membrane in Fig. 5B as well as the cube representations of the volume shown in Fig. 5C,D. Mitochondria are located close to the node of Ranvier, perhaps playing an important role in supplying energy to regenerate membrane potentials after the nerve impulse. In this particular reconstruction, we did not observe the adherens junctions most likely because they are found in the missing segment of the volume, although these are visible in other thick sections from the same sample preparations.

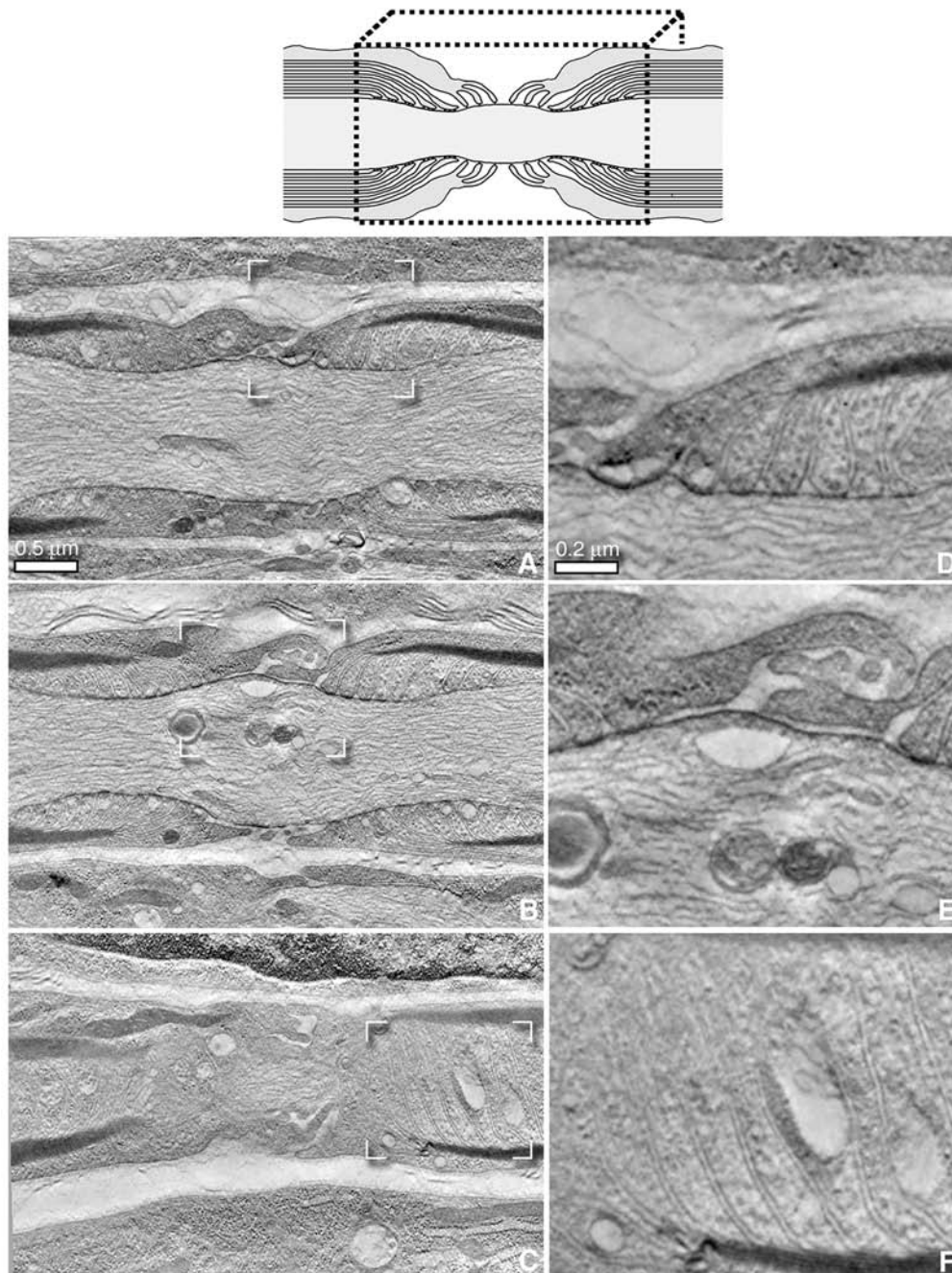


Fig. 4. Serial EMT of a node of Ranvier prepared from a conventionally fixed and HPF dorsal root nerve from a 3-d-old mouse. Top: box on node of Ranvier indicates the 3D location of tomogram. Presented here are slices from each of the three volumes (**A**, **B**, **C**) and higher magnification views of nodal and paranodal areas (**D**, **E**, **F**) denoted by the box corners in (A, B, C). The improvement in ultrastructure can be seen in the smooth, straighter appearance of the membranes and the increase in cytoplasmic contents. Higher magnification views were chosen to illustrate (**D**) microtubules in cross-section in the paranodal loops and dense staining at the glial-axonal septate-like junctions, (**E**) sub-axolemma cisternae and appearance of the Schwann cell body and (**F**) terminations of the paranodal loops over the top of the axon. The magnifications for A, B and C are the same as are D, E and F.

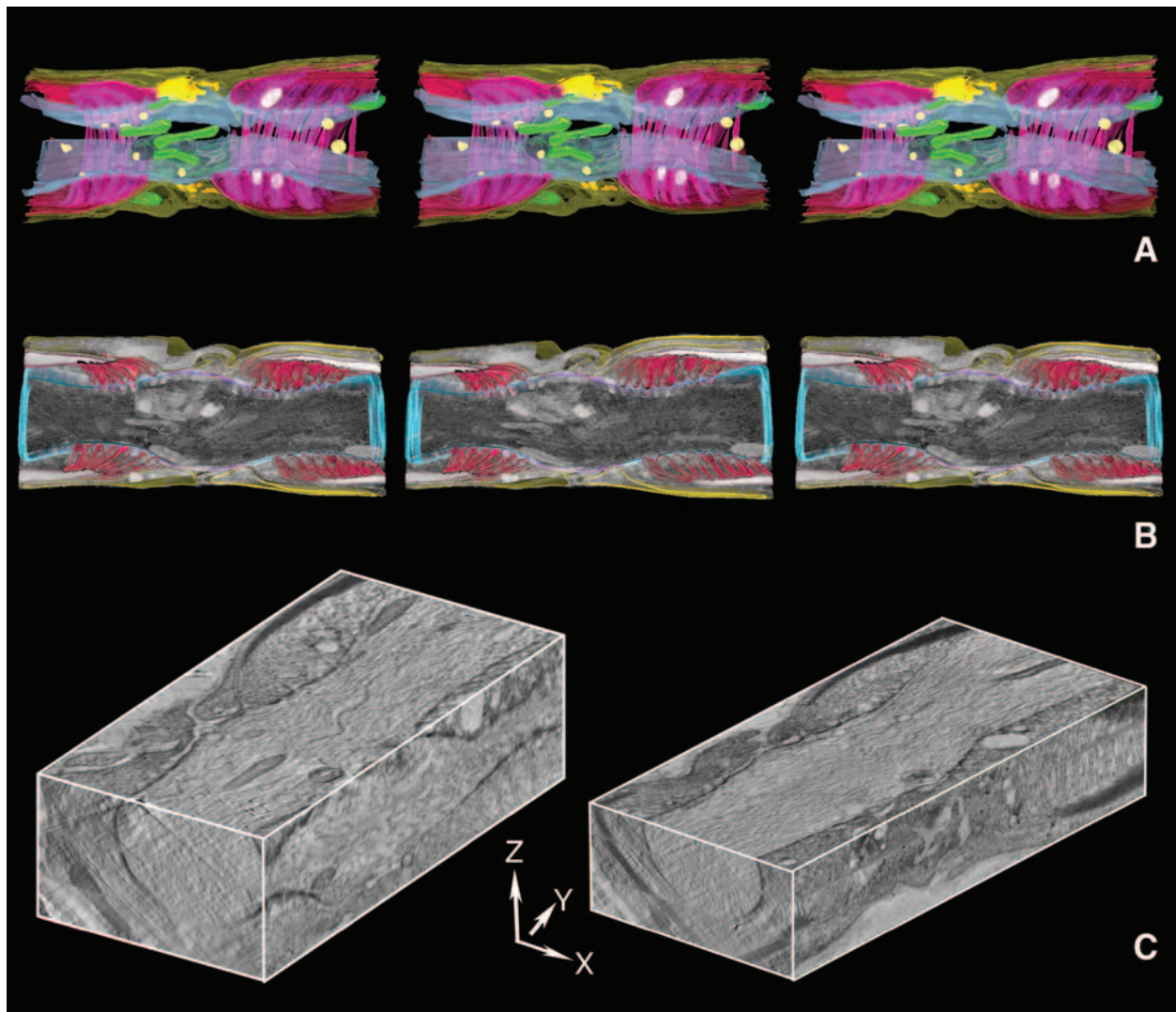


Fig. 5. 3D graphical representations of a serial tomogram of the HPF node of Ranvier. **(A)** The volume shown in Fig. 4 was segmented for membrane compartments. Presented here is a stereo pair surface rendering of the serial tomogram. The stereo images are presented as cross-eyed (left pair) or wall-eyed (right pair). See the legend for Fig. 3 for directions for merging stereo pairs. Again, the outer Schwann cell layer is shown in transparent yellow with the microvilli in gold, the paranodal loops in alternating pink and magenta, mitochondria are green, the paranodal cisternae in gray, lysosomes in light yellow. The axolemma is represented in transparent blue. **(B)** A central slice is shown with surfaces defined as in (A) and containing a volume rendering of the cytoplasmic matrix and cytoskeletal elements. A stereo pair of this combined surface and volume rendering is shown. **(C)** Two cube representations of the volumes to show xy , yz , and xz slices.

Building More Realistic Functional Models Based on Tomographic Reconstruction

Biological structures such as the node of Ranvier are tremendously complex at the sub-

cellular level. Previous theoretical models of ligand diffusion and chemical reactions needed to be simplistic because of the limitations of computational power and did not account for

the actual structure of the neuron or any surrounding glial cells. The simulation program, MCell (MCell= Monte Carlo simulator of Cellular Microphysiology, <http://www.mcell.cnl.salk.edu>, Bartol et al., 1991; Stiles and Bartol, 2001; Stiles et al., 2001), is based on Monte Carlo algorithms and allows highly realistic 3D reconstructions to be incorporated with models of ligand diffusion and receptor activation. For example, this program has been used to simulate neurotransmitter exocytosis at the neuromuscular junction and miniature endplate current generation (Stiles and Bartol, 2001; Stiles et al., 2001) and NMDA and AMPA receptor response to the release of glutamate at central glutamatergic synapses (Franks et al., 2002). Its creation and development have been made possible by the vast improvements in computational power in the last 5 yr. In MCell simulations, the diffusion of individual ligand molecules within an arbitrarily complex 3D environment is simulated using a grid-free Brownian dynamics random walk algorithm. Bulk solution rate constants are converted into Monte Carlo probabilities so that the diffusing ligands react stochastically with respect to individual binding sites, such as receptor proteins, as well as enzymes, transporters, and ion channels. MCell achieves such generality through the use of a Model Description Language (MDL) that allows one to define, in familiar biological terminology, the chemical reaction networks involving ligands and effector molecules and to precisely distribute and organize these components within 3D reconstructions of cellular ultrastructure. Defining a realistic model requires an accurate reconstruction and the spatial distribution of relevant molecules as well as knowledge of the reactions, kinetic rate constants, diffusion constants, ion channel conductances, transport and other biophysical properties pertaining to these molecules.

A requirement for MCell is that closed and continuous membranes bound discrete spatial compartments. Fig. 6 illustrates how a tomo-

graphic 3D structure is used as a starting basis for building a functional model from the HPF node because the reconstruction did not contain the entire node of Ranvier, it was necessary to create a closed membrane model by symmetrizing around the axonal axis. At low resolution, the idealized nerve structure has a mirror plane parallel to the axonal axis. The original model was asymmetric in that one half of the node was more complete than the other. We created a new volume beginning from the side that had the most complete part of the node to the widest point of the axolemma. The volume was duplicated and mirror symmetrized. This partner volume was then merged with the original half-node volume. This new volume was then re-traced for MCell modeling. At the outer parts of the reconstructions where the paranodal loops fuse and Schwann cell contours may be incomplete, connections were approximated to ensure that the models would contain closed surfaces. The surface renderings in Fig. 6A–C reflect the outer to inner compartments in the node that are defined by the Schwann cell membrane (in semi-transparent yellow), compact myelin (pink), paranodal loops (magenta) and axolemma (blue green). The node region is defined between the first paranodal loops of the two myelinating Schwann cells and has been rendered dark blue. In these computer graphic visualizations, the helical nature of the paranodal loops is readily apparent.

Adding Molecular Details Regarding Distributions and Localization of Na⁺ Channels to 3D Models of the Nodal Membrane

Inputs for MCell modeling of the node are: (1) A refined segmented high-resolution tomogram of the tissue at 10 x 10 x 10 nm resolution; (2) a 3D definition of the coordinates of axonal and myelin membranes as well as any impinging surrounding membranes as discrete compartments resolved by the tomogram; (3)

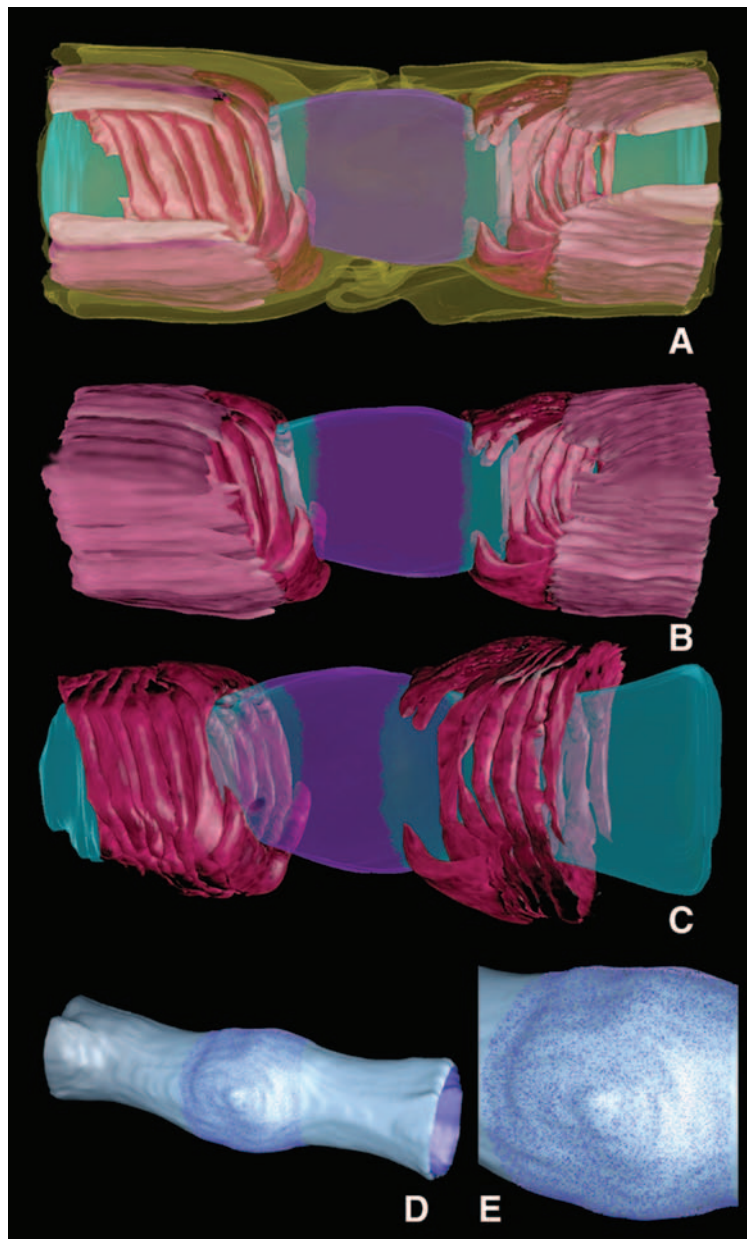


Fig. 6. Node of Ranvier tomographic structure is used for input to adding sodium channel distributions. A 3D model was constructed to approximate the cylindrical symmetry and membrane compartments of the nodal membrane. **(A)** Complete structure containing Schwann cell membrane (transparent yellow), compact myelin (pink), paranodal loops (magenta), axonal membrane (blue green). The nodal part of the axolemma is highlighted in dark blue. **(B)** Similar view as in (A) but the Schwann cell has been removed in order to view the wrapping of the paranodal loops. **(C)** Similar to (B) except that the compact myelin has now been removed. In this slightly tilted view, the helical nature of the wrapping of the paranodal loops is revealed. **(D)** This surface reconstruction of a complete axon was prepared for modeling with MCell. Individual sodium channels have been “painted” on the structure in the location and density determined from multiple experimental studies (e.g., (Ritchie and Rogart, 1977)). **(E)** Higher magnification view showing the close packing and distribution of the sodium channels (as approximated by spheres).

density and spatial distribution of each channel type associated with the reconstructed membrane complex; (4) voltage-dependent kinetic rate constants for each channel type and (5) internal and external ion concentrations at rest. The structural data is obtained from the tomogram of HPF prepared specimens while preliminary information on ion channel density is based on the published estimates for the number of sodium channels.

To begin introducing molecular complexity into our node of Ranvier structure, we added onto the axolemma surface the distribution and density of Na⁺ channels. The precise distribution of these channels was determined by immunoelectron microscopy using Na⁺ channel specific antisera (Ellisman and Levinson, 1982) and the density of the channels was based on estimates from ³H saxitoxin binding experiments on sciatic nerve extracts (Ritchie and Rogart, 1976; Ritchie and Rogart, 1977) or from patch clamping and Na⁺ current analysis of demyelinated sciatic nerves (Shrager, 1989) and estimates of the dimensions of the molecule from (Agnew et al., 1983). Estimates from these studies range from 400-2000/μm², however, we used the 2000/μm² as input based on observations of the density of intramembranous particles in freeze-fracture electron micrographs of the nodal membrane (Ellisman, 1979, (Black et al., 1982; Ellisman et al., 1984; Rosenbluth, 1976; Wiley-Livingston and Ellisman, 1981). The nodal axolemma is easily defined in our tomographic reconstructions and using DReAMM (<http://www.mcell.psc.edu/DReAMM>), part of the MCell/DReAMM microphysiology modeling environment MCell (URL is <http://www.mcell.cnl.salk.edu>). The region was identified within the MCell simulation environment and labeled for mapping and visualization of Na⁺ channels (blue spheres in Figs. 7D and E, corresponding to the dark blue areas in Figs 7A–C). In future experiments, various K⁺ channel isoforms, co-transporters and other ion channels will be added to the model using DReAMM to

simulate transmission of the action potential including activation and deactivation of the ion channels, and accumulation and depletion of ions in the nodal region.

Direct Visualization of Macromolecular Complexes Within the Paranodal Area

New insights into nodal functional mechanisms come from new imaging methods combined with detailed localization studies to determine the distribution of specific macromolecular components within the complex. For example, proteins within the septate-like junctions have been identified (Bhat et al., 2001; Boyle et al., 2001; Dupree et al., 1999; Kazarinova-Noyes et al., 2001; Poliak et al., 2001; Venken et al., 2001). In a unique heterologous synergy, the glial cell contributes neurofascin155 while the neuronal cell contributes caspr1 (Poliak et al., 2001), however, the number of copies of the protein within the complex is still to be determined. Contactin from the neuron serves to target the other proteins to the glial-axonal contact sites (Boyle et al., 2001). We were interested in the direct visualization of fine morphological features, such as these septate-like junctions, that consist of macromolecular complexes and to localize and image these protein complexes in situ at a higher resolution than is afforded by confocal microscopy or standard immuno-EM methodologies.

A region of the paranode from the HPF prepared material was selected for higher magnification double-tilt tomographic reconstruction (CCDB Record ID: node2x). Two orthogonal tilt series, each consisting of 61 images were recorded at 40,000 magnification. The first tomogram in which the tilt axis was perpendicular to the axonal axis was recorded first while the tilt axis was parallel to the axonal axis in the second tomogram. The resolution of the 3D reconstruction is non-isotropic since it is optimal along the tilt axis and worst in the direction perpendicular to the tilt axis. The main

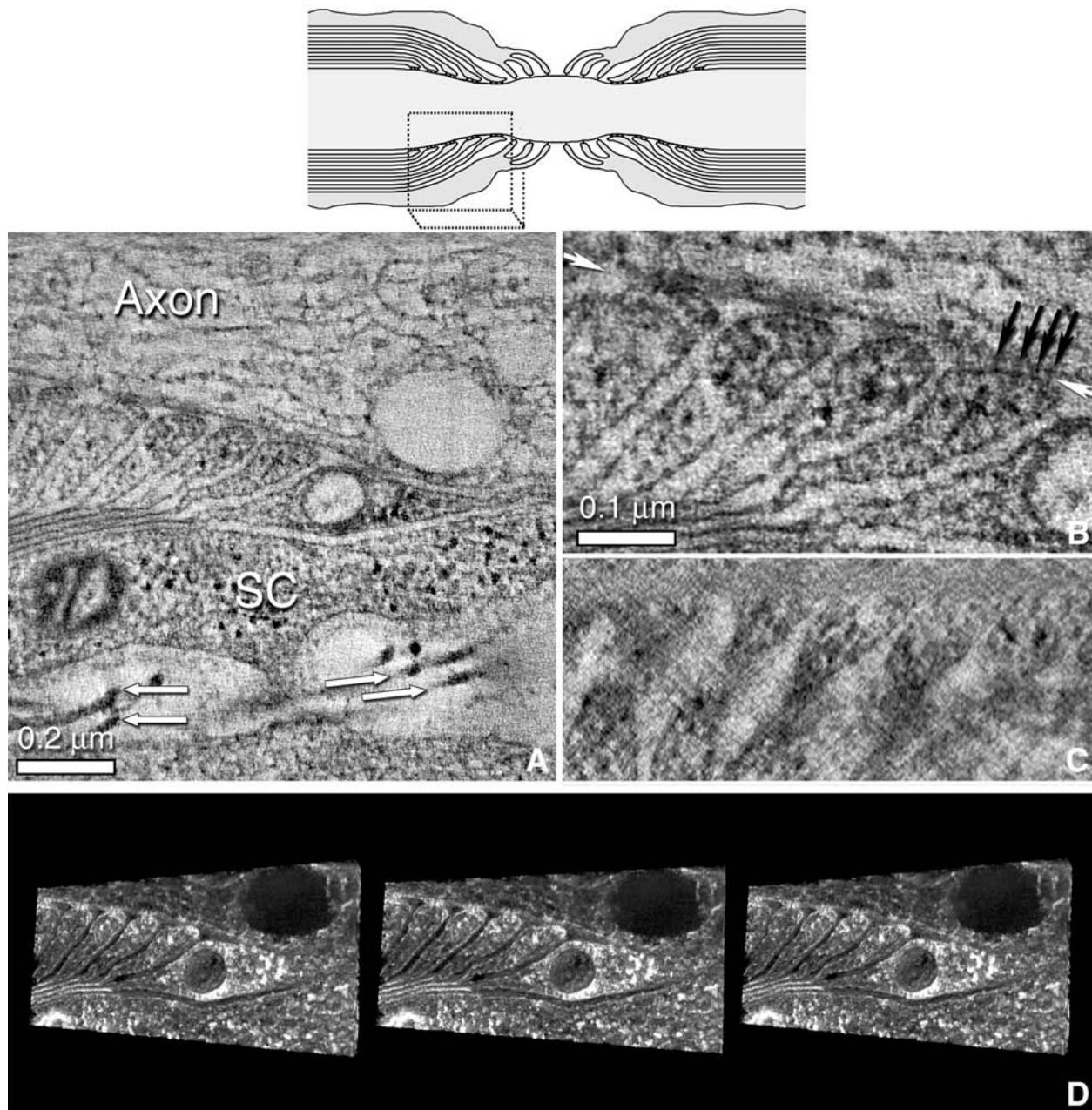


Fig. 7. Higher resolution imaging of a paranodal area illustrating the macromolecular “pegs” joining the glial–axonal junction. Top: box on node schematic indicates tomographic volume. **(A)** A slice from a tomogram recorded at 40,000 magnification of just one set of paranodal loops from dorsal root nerves that had been HPF and imaged with EMT. The axon and Schwann cell body (SC) are marked on image for orientation purposes. The arrows point to individual collagen fibrils that are part of the extracellular matrix surrounding each peripheral nerve. In this slice, the collagen fibrils appear unconnected, however, other sections show these as two continuous fibrils that run the length parallel to the long axis of the Schwann cell body. Each slice in this reconstruction is approx 15 Å thick. **(B)** Higher magnification (2X) view of the first four paranodal loops. The arrow points to a set of septate-like junction “pegs” in the glial-axonal junctional domain. **(C)** This volume was re-oriented and interpolated so

effect of merging the two orthogonal volumes is that there is now symmetry in resolution between the directions in the two slices. For example, the membranes in paranodal cisternae that have circular profiles will appear crisp around their circumference (*see* the cisterna in first paranodal loop of Fig. 7A) whereas in the individual volumes these membranes appear less sharply defined in the direction perpendicular to the tilt axis (*see* online animation at <https://ccdb.ucsd.edu/CCDB/animationprofile.htm> with link to node 2x). This tomogram defines in 3D the macromolecular “pegs” joining the glial–axonal junction seen in previous deep etched rotary shadowed preparations (Ichimura and Ellisman, 1991). These glial–axonal junctions measure approx 20–25 nm in diameter and approx 5–6 nm in length in this reconstruction as measured in the higher magnification view of the x-y slice (Fig. 7B) as well as measurements from an oblique section that runs through the septate-like junctions parallel to the axolemma. In this tomogram, the approx 20 nm repeat of the collagen fibril is clear (data not shown). This section provides a unique view down onto the membrane plane and septate-like junction “pegs”. The banding pattern in this slice arises from the curved end of the four paranodal loops as they join the junctional areas. From the area shown in Fig. 7B, a sub-volume was windowed to only 50 x-y slices (~76 nm thick). The original tomogram contained 200 x-y slices. This was then volume rendered and is shown in stereo in Fig. 7D in order to convey the 3D structure and orientation of the pegs and their connections to cytoskeletal elements in both the paranodal loops and the axon.

Discussion

Numerous studies (Carley and Raymond, 1987; Endres et al., 1986; Halter and Clark, 1993; Lev-Ram and Ellisman, 1995; Lev-Ram and Grinvald, 1986; Lev-Ram and Grinvald, 1987; Murray and Steck, 1984; Wurtz and Ellisman, 1986) support the idea that the axon/myelin/glia cell ensemble or “nodal complex” operates in an integrated manner during conduction of the nerve impulse. This is particularly striking in cases of human hereditary neuropathies such as Charcot-Marie-Tooth (CMT) disease where disruption of the myelin structure or maintenance causes changes in axonal morphology and nerve impulse conduction (Martini, 2001). Our overall objective is to elucidate the functional interactions between axons and myelinating glia and their constituent proteins to understand more about how the nodal complex manages and modulates propagation of the nerve impulse. As a first step, we have extracted new information about the structural organization of the node using EMT imaging and volume reconstruction upon which more accurate models can be built. Recent studies from this laboratory on the distribution, kinetics and microphysiology of acetylcholine receptor isoforms using a serial section tomographic volume of the chick ciliary ganglion (Shoop et al., 2002) as a starting model for the MCell environment has demonstrated that a computational model of synaptic transmission with nanometer precision and microsecond accuracy replicates complex synaptic events and reveals functional extracellular micro-domains (Esquenazi et al., 2001). These studies serve as a precedent for the more

that the transverse principal axis was along the line defined by the white arrows in (B). The slice that goes through the septate-like-junctions and loops is shown here and is the view that one would see if looking down on the paranodal loops from the axolemma. In this orientation, the five loops appear as bands with dense striations from the septate-like junction pegs seen end on. The magnification for (C) is the same as for (B). (D) A stereo pair of the sub-volume of the area presented in (B) with only 50 sections. The stereo images are presented as cross-eyed (left pair) or wall-eyed (right pair). See the legend for Fig. 3 for directions for merging stereo pairs.

complex task of creating computational models of node microphysiology for which having accurate, complex closed surface compartmentalized models derived from tomographic reconstructions and containing information about the location and packing of key molecules are absolutely necessary as a starting point for developing the necessary parameters for the simulation environment.

Organization of Membrane Compartments Within the Nodal Complex

The node of Ranvier is one of the most compartmentalized multicellular complexes. Each of the membrane systems, e.g. axonal, glial cell body, paranodal loops, internal cisternae and microvilli, define a three-dimensional space with its own unique set of ions, metabolites and proteins. During the propagation of an action potential, large amounts of ions are transiently released. The key to maintaining the homeostasis of the nodal complex is the transporting of Na^+ , K^+ and counter-ions across the constituent membranes. The Schwann cell microvilli are dynamic structures (Wurtz and Ellisman, 1986) that are mostly likely moving in and out of the nodal gap (Gatto et al., 2003) and therefore, the structures presented here provide a "snapshot" of the microvilli at the time of specimen preparation. It is important to note that the energy load from maintaining the electrical balance is probably quite large and mitochondria often appear not only in the axon at or close to the Node of Ranvier, but also within paranodal loops and Schwann cells. Whether mitochondria near to the node are more actively respiring as compared to those further away is an investigation currently underway.

The accurate depiction of the membranes depends not only on the quality of the imaging, but especially on the method used for preserving the specimens. Here, we have used HPF and freeze substitution in conjunction with aldehyde fixation to optimize the struc-

tural preservation. Large, internal tissue masses such as brain or nerve tissue are acutely sensitive to anoxia and the tradeoff that one must make is whether any artifacts due to aldehyde fixation are worse than the tissue and cell damage occurring upon anoxia during dissection and removal of the tissue. Since an important goal of this tomographic study is to provide a structural basis for modeling the action potential, it is critical to define the membrane systems accurately.

Closed cisternal compartments provide a means by which the axonal and glial cells can sequester ions and other small molecules. Small cisternae and axonal smooth SER are visualized in the 3D reconstructions lying just underneath the axolemma parallel to the long axis of the axon. These subsurface cisternae have been shown to be connected to the axolemma via thin filamentous structures (Ichimura and Ellisman, 1991) that are part of a membrane-cytoskeletal linker system. In contrast, tubular cisternae run perpendicular to this axis throughout the extent of the paranodal loops and also are anchored by paranodal cytoskeletal elements to the loop membrane. The paranodal loops form a continuous helical compartment contiguous with the glial cell body. These paranodal cisternae have the appearance of "fingers" and may serve as a storehouse of metabolites. In fact, it has been hypothesized that the cause and effect of the X-linked Charcot-Marie-Tooth (CMTX) disease is that reflexive gap junctions found in the paranodal area are deficient or non-functional and therefore cannot pass metabolites from internal stores within the paranodal loops (Paul, 1995). In essence, the gap junctions may form a type of "shortcut" for rapid diffusion of metabolites. The elegant interplay between the membrane compartments and cytoskeletal network provide a mechanical link between the individual glial and axonal cytoskeleton stabilizing the three-cell complex particularly during the action

potential when high ion fluxes occur (Ichimura and Ellisman, 1991).

The Role of Cell–Cell Junctions in Maintaining the Compartmentalization of the Nodal Complex

The nodal complex is rich in different types of inter- and intra-cellular junctions. Cell-cell junctions are formed between homologous cells (tight junctions, gap junctions, and adherens in the paranode) as well as between heterologous cells (septate-like junctions). The septate-like junctions act in a paracellular capacity to block diffusion of ions into the paranodal and juxtanodal areas (Salzer, 2003). By immunofluorescence, the paranodal regions of nodes of Ranvier have been shown to contain high levels of connexin32, presumably making reflexive junctions (Paul, 1995) and lower amounts of connexin29 (Altevogt et al., 2002). However, while we could resolve the septate-like junctions, some tight junctions and adherens junctions, we could not find any canonical “pentalaminar” gap junction profiles. These reflexive junctions provide an important metabolic channel and defects in the sequence of connexin32 lead to direct myelin pathologies in CMTX diseases (Ionasescu, 1995; Scherer et al., 1999). Since we are able to resolve 20–25 nm septate-like junctions, the most likely explanation is that connexin channels do not form large or closely packed plaques as they do in other tissues such as heart, liver or pancreas. An alternative explanation is that in the young animals we used in this study these junctions are small and located at oblique angles to the principal Cartesian coordinate axes (Altevogt et al., 2002).

The combination of adherens junctions and tight junctions are thought to play a role in maintaining the structural integrity of the paranodal area but also serve to facilitate and/or restrict mobility of ions and other diffusible substances. This issue is particularly important

for structures such as ion channels whose density must be very precisely regulated. Recent studies have shown that adherens and tight junction proteins (β -catenin, ZO-1, ZONAB, and huASH1) are active partners in signaling pathways that regulate cell growth and differentiation by either interacting with or acting as transcription factors (Balda and Matter, 2000; Kirkpatrick and Peifer, 1995; Nakamura et al., 2000; Tsukita et al., 1999). Adherens junctions are one of the larger junctional structures in the node of Ranvier and occur in one continuous structure that is highly localized. In one of our reconstructions, it is obvious that adherens junctions anchor the myelin lateral loops to one another in a continuous belt, acting as a stabilizing influence on the membranes. While these adherens junctions were apparent in only one of our tomograms, it is likely that all nodal complexes have them and these junctions may have been located in the missing 20–25% portion of the reconstruction.

Septate-like junctions serve to anchor the myelinating glial paranodal loops to the axonal membrane. This structure is unique in that the two cell types (neuron and glial cell) both contribute membrane proteins and cytoskeletal elements that form a highly structured macromolecular complex. Organized arrays of particles were described in the paranodal region forming the glial-axonal-junction in freeze fracture electron micrographs (Ellisman, 1979; Wiley and Ellisman, 1980; Wiley-Livingston and Ellisman, 1981). Disruption of the septate-like junctions has a direct impact on action potential transmission as evidenced by a decrease in conduction velocities (Bhat et al., 2001; Boyle et al., 2001). Here we have shown that we can directly image the septate-like junction pegs and that these are most likely the particles seen in freeze-fracture. What can also be seen in our reconstructions is that cytoskeletal elements are attached on both the glial and axonal membranes that serve to anchor the septate-like

junctions in place. Such a constraint will be built into future models.

Organization of Ion Channels Within the Node of Ranvier

From these serial tomograms, we have analyzed and integrated information about ion channel types, isotypes and organization, we can start to build better 3D models of the node of Ranvier. Such a starting step in the modeling process is shown in Fig. 6 by integrating information about domain size and numbers of the voltage-gated Na⁺ channels from the literature into the segmented tomographic structure. The presence of high concentrations of voltage-gated Na⁺ channels at nodal axonal membranes was first deduced from physiological studies and rough predictions of the number of channels estimated in ³H saxitoxin binding experiments on nerve extracts (Ritchie and Rogart, 1976; Ritchie and Rogart, 1977). Freeze-fracture replicas of nodes of Ranvier show a remarkable specialization of the axonal membrane molecular architecture with a variety of segregated intramembranous protein particles (Livingston et al., 1973; Schnapp and Mugnaini, 1975; Wiley and Ellisman, 1980). These freeze-fracture data provided additional support for the presence of a high density of Na⁺ channels at the nodal axolemma, since intramembranous particles corresponding to the estimated size of Na⁺ channels were restricted to these sites (Black et al., 1982; Ellisman et al., 1982; Kristol et al., 1978; Rosenbluth, 1976) and are confirmed by immunoelectron microscopy (Ellisman and Levinson, 1982). The density of Na⁺ channels within the nodal membrane is now estimated to be as high as 2000/μm² (Hille, 1992), but the density is most likely to be only 20–25/μm² in the axolemma of the paranodal and internodal regions (Shrager, 1989).

Future models for simulation will need to incorporate additional data about constituent channels and pump proteins. These include the Ryanodine receptor (Ca²⁺ release channel), the

Na⁺ / Ca²⁺ exchanger protein, water channels and distinct voltage-gated Na⁺ and K⁺ channels. In addition, some K⁺ channels are known to be located preferentially in the glial processes. Some glial cells, including Schwann cells, contain voltage dependent ion channels, inward rectifiers and other types of ion channels (Barres, 1991; Chiu, 1991; Mi et al., 1995; Mi et al., 1996; Mi et al., 1999; Waxman and Ritchie, 1993). Associations of Schwann cell microvilli with the nodal membranes of the PNS axons and astrocytes processes with nodal membrane of the CNS axons were described (Ellisman et al., 1987; Ellisman and Porter, 1980). The nodal membrane has also been shown to contain high concentrations of the Na⁺/K⁺ ATPase (Ariyasu et al., 1985; Wood et al., 1977), which is responsible for polarization of the membrane potential.

Structural Differences Between Nodes of Ranvier of Young and Mature Mice

We prepared specimens from young mice for this study. These animals were at least three days old (P3) or seven days old (P7). and while this study has integrated information on the numbers of sodium channels from adult animals, it is important to point out that there may be some differences. Myelin formation in rodents is just commencing at birth. Most developmental studies examining the ultrastructural changes in the nodal region have focused on either rats (Vabnick and Shrager, 1998; Webster, 1971; Webster et al., 1973; Yamamoto et al., 1996) or cats (Berthold, 1996; Sward et al., 1995). From work of others and our own extensive studies of nodal development (Wiley-Livingston and Ellisman, 1980), the development and maturity of nodes of Ranvier is quite similar in mice. Development of the node of Ranvier begins with the formation of nodal clusters, occurring concurrently with or slight before the organization of paranodal junctions and is followed by a concentration of juxtapara-

nodal components (Girault and Peles, 2002; Wiley-Livingston and Ellisman, 1980). In rats, sodium channel clustering is minimal at birth and increases to detectable freeze fracture intramembranous particle clusters (Wiley-Livingston and Ellisman, 1980) or immunostaining levels at days P3–P4 (Vabnick et al., 1996). The number of nodes remains fairly constant however the length of the internodes increases (Berthold and Skoglund, 1968; Wiley-Livingston and Ellisman, 1980). As animals mature, the diameter of the nodal complex increases (Sward et al., 1995) and the paranodal loops become more invested with paranodal loops and septate-like junctions with the eventual development of Bracelets of Nageotte (Yamamoto et al., 1996). In general, adult peripheral nodes of thin fibers can be thought of as equivalent in general structure to young thinly myelinated peripheral nodes. However, with the thickening of myelin on larger fibers, the ultrastructure changes with an increase in the number of myelin terminal loops that attach directly to the axon. The longitudinal length of the axons nodal membrane and the paranodal membrane remains similar regardless of the size or age of the fiber (Berthold et al., 1983). The most dramatic change with development of large fibers is the more complicated structure of the paranodal glial loops investing the paranodal axolemma.

Availability of Models and Data for the Computational Neuroscience Community

The image data and models derived from these represent a first step for incorporating realistic, accurate 3D data into simulation environments such as NEURON or MCell. NEURON is a simulation environment for developing and exercising models of neurons and networks of neurons (URL <http://www.neuron.yale.edu/neuron/>; (Hines and Carnevale, 2001). It is particularly well-suited to problems where cable

properties of cells play an important role, possibly including extracellular potential close to the membrane), where cell membrane properties are complex (as in the node of Ranvier) and involve many ion-specific channels, ion accumulation, and second messengers.

MCell and NEURON are complementary simulation environments that are representative of computational tools for realistic simulation of biological systems. Such tools are made much more useful through the availability of rigorously vetted biological data in machine-readable format. In order to facilitate computational experiments and for dissemination to the scientific community, the original tilt images, volumes and models segmented from the volumes have been made available in the Cell Centered Data Base (CCDB; URL <http://ccdb.ucsd.edu/CCDB/>; (Martone et al., 2004; Martone et al., 2002; Martone et al., 2003) for downloading. The CCDB, a web-accessible database, was designed for dissemination of structural and protein localization information from large expanses of tissue to cellular microdomains with their associated macromolecular constituents. The CCDB makes this 3D microscopic imaging data available to the scientific community. Such a resource is important in the management and integration of 3D structural information with neurophysiological and molecular databases that span the scale of systems neurobiology (Martone et al., 2004). In addition, dissemination of tomographic data allows additional “mining” of information within these highly labor intensive and data-rich volumes. Within this neuroinformatics database, the models can be cross-referenced with other relevant databases, such as those within SenseLab Project (<http://senselab.med.yale.edu/senselab/>). The models we have created are in a machine readable form that can be indexed within the database. In a complex model such as the node of Ranvier, additional partitioning can be done

so individual compartments or domains can be indexed. We have shown that different anatomical domains or regions, such as the part of the nodal membrane containing the bands of sodium channels, can be segmented within the MCELL model. Computational experiments performed with such a model can also be referenced back within the database.

The range of computational experiments that could be envisioned is enormous with increasing the complexity by including multiple parameters in the simulations. Development of new structures promote comparative studies between nerves with physiological/functional differences in a more quantitative manner than before, assessing kinetics, channel types and distributions, compartment sizes, shapes, surface areas, volumes in relation to ion fluxes and excitability and morphological differences. For example, it has been speculated that activity dependent effects would lead to failures at branch points of myelinated axons which ramify extensively in some regions of the CNS and that this phenomenon may play a role in modulation of information flow in the nervous system (c.f. (Wurtz and Ellisman, 1986). Regardless of the impact on branching axons it is known that some nodes are very poor at recovering quickly from repetitive activation and others are designed to manage high frequency firing without contributing to latency shifts. Similar tomographic reconstructions of nerves with different firing frequencies will further test the hypothesis that one way of modulating action potentials is to have nerve structures in which the membrane compartments are structurally different. Deposition of these reconstructions and their segmented models into the CCDB will facilitate longer range, broader structure/function studies.

Supplemental Materials

Online supplemental videos (<https://ccdb.ucsd.edu/CCDB/animationprofile.htm>) are (1) node-video1-sm.mov: animations of the tilt

series, slices in 3D reconstruction and segmented volume of the HPF node Ranvier presented in this paper and (2) node-video2-sm.mov: animation of slices in tomogram of the high resolution paranodal area presented in Fig. 7 and can be accessed as well through record ID numbers in the CCDE.

Acknowledgments

The authors would like to thank Ying Jones for assistance with sectioning and preparation of the HPF samples and Guy Perkins for processing of the double tilt data with IMOD. We also thank Dr. Kent McDonald for his help, expertise and access to the Bal-Tec HPF at UC Berkeley and Dr. Maryann Martone for valuable discussions. This work was supported by National Institutes of Health grant NS14718 (MHE) and National Science Foundation grants MCB 9728338, 0131425 (GES). MCell development and maintenance was supported by National Science Foundation grants IBN-9985964, ITR-0086092, and ASC-97-5249 awarded to Terrence Sejnowski, National Institutes of Health GM068630 awarded to Joel Stiles and the Center for Theoretical Biological Physics (National Science Foundation PHY0225630 awarded to José Onuchic). The work described in this paper was conducted at the National Center for Microscopy and Imaging Research at San Diego, which is supported by NIH Grant RR04050 awarded to M.H.E. The CCDB is supported by National Institutes of Health grant DA016602 (Maryann Martone).

References

- Agnew, W.S., J.A. Miller, M.H. Ellisman, R.L. Rosenberg, S.A. Tomiko, and S.R. Levinson. (1983) The voltage-regulated sodium channel from the electroplax of *Electrophorus electricus*. *Cold Spring Harb Symp Quant Biol.* 48 Pt 1:165–79.
- Altevogt, B.M., K.A. Kleopa, F.R. Postma, S.S. Scherer, and D.L. Paul. (2002) Connexin29 is uniquely distributed within myelinating glial cells of the central and peripheral nervous systems. *J Neurosci.* 22:6458–70.

- Alvarez-Leefmans, F.J., M. Leon-Olea, J. Mendoza-Sotelo, F.J. Alvarez, B. Anton, and R. Garduno. (2001) Immunolocalization of the Na(+)-K(+)-2Cl(-) cotransporter in peripheral nervous tissue of vertebrates. *Neuroscience*. 104:569–82.
- Ariyasu, R.G., J.A. Nichol, and M.H. Ellisman. (1985) Localization of sodium/potassium adenosine triphosphatase in multiple cell types of the murine nervous system with antibodies raised against the enzyme from kidney. *J Neurosci*. 5:2581–96.
- Balda, M.S., and K. Matter. (2000) The tight junction protein ZO-1 and an interacting transcription factor regulate ErbB-2 expression. *Embo J*. 19:2024–33.
- Barres, B.A. (1991) New roles for glia. *J Neurosci*. 11:3685–94.
- Bartol, T.M., Jr., B.R. Land, E.E. Salpeter, and M.M. Salpeter. (1991) Monte Carlo simulation of miniature endplate current generation in the vertebrate neuromuscular junction. *Biophys J*. 59:1290–307.
- Bergoffen, J., S.S. Scherer, S. Wang, M. Oronzi Scott, L.J. Bone, D.L. Paul, K. Chen, M.W. Lensch, P.F. Chance, and K.H. Fischbeck. (1993) Connexin mutations in X-linked Charcot-Marie-Tooth disease. *Science*. 262:2039–2042.
- Berthold, C.H. (1996) Development of nodes of Ranvier in feline nerves: an ultrastructural presentation. *Microsc Res Tech*. 34:399–421.
- Berthold, C.H., I. Nilsson, and M. Rydmark. (1983) Axon diameter and myelin sheath thickness in nerve fibres of the ventral spinal root of the seventh lumbar nerve of the adult and developing cat. *J Anat*. 136 (Pt 3):483–508.
- Berthold, C.H., and S. Skoglund. (1968) Postnatal development of feline paranodal myelin-sheath segments. II. Electron microscopy. *Acta Soc. Med. Ups*. 73:127–144.
- Bhat, M.A., J.C. Rios, Y. Lu, G.P. Garcia-Fresco, W. Ching, M. St Martin, J. Li, S. Einheber, M. Chesler, J. Rosenbluth, J.L. Salzer, and H.J. Bellen. (2001) Axon-glia interactions and the domain organization of myelinated axons requires neurexin IV/Caspr/Paranodin. *Neuron*. 30:369–83.
- Black, J.A., R.E. Foster, and S.G. Waxman. (1982) Rat optic nerve: freeze-fracture studies during development of myelinated axons. *Brain Res*. 250:1–20.
- Boyle, M.E., E.O. Berglund, K.K. Murai, L. Weber, E. Peles, and B. Ranscht. (2001) Contactin orchestrates assembly of the septate-like junctions at the paranode in myelinated peripheral nerve. *Neuron*. 30:385–97.
- Carley, L.R., and S.A. Raymond. (1987) Comparison of the after-effects of impulse conduction on threshold at nodes of Ranvier along single frog sciatic axons. *J Physiol*. 386:503–27.
- Chiu, S.Y. (1991) Functions and distribution of voltage-gated sodium and potassium channels in mammalian Schwann cells. *Glia*. 4:541–58.
- Dahl, R., and L.A. Staehelin. (1989) High-pressure freezing for the preservation of biological structure: theory and practice. *J Electron Microsc Tech*. 13:165–74.
- Dupree, J.L., J.A. Girault, and B. Popko. (1999) Axo-glia interactions regulate the localization of axonal paranodal proteins. *J Cell Biol*. 147:1145–52.
- Ellisman, M.H. (1979) Molecular specializations of the axon membrane at nodes of Ranvier are not dependent upon myelination. *J Neurocytol*. 8:719–35.
- Ellisman, M.H., W.S. Agnew, J.A. Miller, and S.R. Levinson. (1982) Electron microscopic visualization of the tetrodotoxin-binding protein from *Electrophorus electricus*. *Proc Natl Acad Sci U S A*. 79:4461–5.
- Ellisman, M.H., and S.R. Levinson. (1982) Immunocytochemical localization of sodium channel distributions in the excitable membranes of *Electrophorus electricus*. *Proc Natl Acad Sci U S A*. 79:6707–11.
- Ellisman, M.H., D.E. Palmer, and M.P. Andre. (1987) Diagnostic levels of ultrasound may disrupt myelination. *Exp Neurol*. 98:78–92.
- Ellisman, M.H., and K.R. Porter. (1980) Microtubular structure of the axoplasmic matrix: visualization of cross-linking structures and their distribution. *J Cell Biol*. 87:464–79.
- Ellisman, M.H., C.A. Wiley, J.D. Lindsey, and C.C. Wurtz. (1984) Structure and function of the cytoskeleton and endomembrane systems at the node of Ranvier. In *The Node of Ranvier*. J. Zagroen and S. Federoff, editors. Academic Press, New York. 153–181.
- Endres, W., P. Grafe, H. Bostock, and G. ten Bruggencate. (1986) Changes in extracellular pH during electrical stimulation of isolated rat vagus nerve. *Neurosci Lett*. 64:201–5.
- Esquenazi, E., J.S. Coggan, T.M. Bartol, R.D. Shoop, T.J. Sejnowski, M.H. Ellisman, and D.K. Berg. (2001) Computer simulation of synaptic ultrastructure and microphysiology in the chick ciliary ganglion. *Society for Neuroscience Abstract*.
- Fan, G.Y., S.J. Young, T. Deerinck, and M.H. Ellisman. (1996) A new electron-optical mode for high con-

- trast imaging and online stereo observation in TEM. *Journal of the Microscopy Society of America*. 2:137–146.
- Fannon, A.M., D.L. Sherman, G. Ilyina-Gragerova, P.J. Brophy, V.L. Friedrich, Jr., and D.R. Colman. (1995) Novel E-cadherin-mediated adhesion in peripheral nerve: Schwann cell architecture is stabilized by autotypic adherens junctions. *J Cell Biol*. 129:189–202.
- Fawcett, J.W., and R.J. Keynes. (1990) Peripheral nerve regeneration. *Annu Rev Neurosci*. 13:43–60.
- Frank, J. (1989) Image analysis of single macromolecules. *Electr.Microsc.Rev*. 2:53–74.
- Franks, K.M., T.M. Bartol, Jr., and T.J. Sejnowski. (2002) A Monte Carlo model reveals independent signaling at central glutamatergic synapses. *Biophys J*. 83:2333–48.
- Gatto, C.L., B.J. Walker, and S. Lambert. (2003) Local ERM activation and dynamic growth cones at Schwann cell tips implicated in efficient formation of nodes of Ranvier. *J Cell Biol*. 162:489–98.
- Gillespie, C.S., D.L. Sherman, G.E. Blair, and P.J. Brophy. (1994) Periaxin, a novel protein of myelinating Schwann cells with a possible role in axonal ensheathment. *Neuron*. 12:497–508.
- Girault, J.A., and E. Peles. (2002) Development of nodes of Ranvier. *Curr Opin Neurobiol*. 12:476–85.
- Griffin, J.W., C.Y. Li, C. Macko, T.W. Ho, S.T. Hsieh, P. Xue, F.A. Wang, D.R. Cornblath, G.M. McKhann, and A.K. Asbury. (1996) Early nodal changes in the acute motor axonal neuropathy pattern of the Guillain-Barre syndrome. *J Neurocytol*. 25:33–51.
- Halter, J.A., and J.W. Clark, Jr. (1993) The influence of nodal constriction on conduction velocity in myelinated nerve fibers. *Neuroreport*. 4:89–92.
- Harlow, M.L., D. Ress, A. Stoschek, R.M. Marshall, and U.J. McMahan. (2001) The architecture of active zone material at the frog's neuromuscular junction. *Nature*. 409:479–84.
- Hille, B. (1992) *Ionic Channels of Excitable Membranes*. Sinauer Associates, Sunderland, MA.
- Hines, M.L., and N.T. Carnevale. (2001) NEURON: a tool for neuroscientists. *Neuroscientist*. 7:123–35.
- Ichimura, T., and M.H. Ellisman. (1991) Three-dimensional fine structure of cytoskeletal-membrane interactions at nodes of Ranvier. *J Neurocytol*. 20:667–81.
- Ionasescu, V.V. (1995) Charcot-Marie-Tooth neuropathies: From clinical description to molecular genetics. *Muscle and Nerve*. 18:267–275.
- Kazarinova-Noyes, K., J.D. Malhotra, D.P. McEwen, L.N. Mattei, E.O. Berglund, B. Ranscht, S.R. Levinson, M. Schachner, P. Shrager, L.L. Isom, and Z.C. Xiao. (2001) Contactin associates with Na⁺ channels and increases their functional expression. *J Neurosci*. 21:7517–25.
- Kirkpatrick, C., and M. Peifer. (1995) Not just glue: cell-cell junctions as cellular signaling centers. *Curr Opin Genet Dev*. 5:56–65.
- Kremer, J.R., D.N. Mastronarde, and J.R. McIntosh. (1996) Computer visualization of three-dimensional image data using IMOD. *J Struct Biol*. 116:71–6.
- Kristol, C., C. Sandri, and K. Akert. (1978) Intramembranous particles at the nodes of Ranvier of the cat spinal cord: a morphometric study. *Brain Res*. 142:391–400.
- Ladinsky, M.S., J.R. Kremer, R.S. Furcinitti, J.R. McIntosh, and K.E. Howell. (1994) HVEM tomography of the trans-Golgi network: structural insights and identification of a lace-like vesicle coat. *J Cell Biol*. 127:29–38.
- Lambert, S., J.Q. Davis, and V. Bennett. (1997) Morphogenesis of the node of Ranvier: co-clusters of ankyrin and ankyrin-binding integral proteins define early developmental intermediates. *J Neurosci*. 17:7025–36.
- Lenzi, D., J.W. Runyeon, J. Crum, M.H. Ellisman, and W.M. Roberts. (1999) Synaptic vesicle populations in saccular hair cells reconstructed by electron tomography. *J Neurosci*. 19:119–32.
- Lev-Ram, V., and M.H. Ellisman. (1995) Axonal activation-induced calcium transients in myelinating Schwann cells, sources, and mechanisms. *J Neurosci*. 15:2628–37.
- Lev-Ram, V., and A. Grinvald. (1986) Ca²⁺- and K⁺-dependent communication between central nervous system myelinated axons and oligodendrocytes revealed by voltage-sensitive dyes. *Proc Natl Acad Sci U S A*. 83:6651–5.
- Lev-Ram, V., and A. Grinvald. (1987) Activity-dependent calcium transients in central nervous system myelinated axons revealed by the calcium indicator Fura-2. *Biophys J*. 52:571–6.
- Livingston, R.B., K. Pfenniger, H. Moor, and K. Akert. (1973) Specialized paranodal and interparanodal glial-axonal junctions in the peripheral and central nervous system: a freeze-etching study. *Brain Res*. 58:1–24.
- Mannella, C.A., M. Marko, P. Penczek, D. Barnard, and J. Frank. (1994) The internal compartmentation of rat-liver mitochondria: tomographic study using the high-voltage transmission electron microscope. *Microsc Res Tech*. 27:278–83.

- Marsh, B.J., D.N. Mastronarde, K.F. Buttle, K.E. Howell, and J.R. McIntosh. (2001) Organellar relationships in the Golgi region of the pancreatic beta cell line, HIT-T15, visualized by high resolution electron tomography. *Proc Natl Acad Sci U S A.* 98:2399–406.
- Martin, S., A.K. Levine, Z.J. Chen, Y. Ughrin, and J.M. Levine. (2001) Deposition of the NG2 proteoglycan at nodes of Ranvier in the peripheral nervous system. *J Neurosci.* 21:8119–28.
- Martini, R. (2001) The effect of myelinating Schwann cells on axons. *Muscle Nerve.* 24:456–66.
- Martone, M.E., A. Gupta, and M.H. Ellisman. (2004) E-neuroscience: challenges and triumphs in integrating distributed data from molecules to brains. *Nat Neurosci.* 7:467–72.
- Martone, M.E., A. Gupta, M. Wong, X. Qian, G. Sosinsky, B. Ludascher, and M.H. Ellisman. (2002) A cell-centered database for electron tomographic data. *J Struct Biol.* 138:145–55.
- Martone, M.E., Y.Z. Jones, S.J. Young, M.H. Ellisman, J.A. Zivin, and B.R. Hu. (1999) Modification of postsynaptic densities after transient cerebral ischemia: a quantitative and three-dimensional ultrastructural study. *J Neurosci.* 19:1988–97.
- Martone, M.E., S. Zhang, A. Gupta, X. Qian, H. He, D.L. Price, M. Wong, S. Santini, and M.H. Ellisman. (2003) The cell-centered database: a database for multiscale structural and protein localization data from light and electron microscopy. *Neuroinformatics.* 1:379–95.
- Mastronarde, D.N. (1997) Dual-axis tomography: an approach with alignment methods that preserve resolution. *J Struct Biol.* 120:343–52.
- Maxwell, W.L., A. Irvine, Graham, J.H. Adams, T.A. Gennarelli, R. Tipperman, and M. Sturatis. (1991) Focal axonal injury: the early axonal response to stretch. *J Neurocytol.* 20:157–64.
- McDonald, K. (1999) High-pressure freezing for preservation of high resolution fine structure and antigenicity for immunolabeling. *Methods Mol Biol.* 117:77–97.
- Medalia, O., I. Weber, A.S. Frangakis, D. Nicastro, G. Gerisch, and W. Baumeister. (2002) Macromolecular architecture in eukaryotic cells visualized by cryoelectron tomography. *Science.* 298:1209–13.
- Melendez-Vasquez, C.V., J.C. Rios, G. Zanazzi, S. Lambert, A. Bretscher, and J.L. Salzer. (2001) Nodes of Ranvier form in association with ezrin-radixin-moesin (ERM)-positive Schwann cell processes. *Proc Natl Acad Sci U S A.* 98:1235–40.
- Mi, H., T.J. Deerinck, M.H. Ellisman, and T.L. Schwarz. (1995) Differential distribution of closely related potassium channels in rat Schwann cells. *J Neurosci.* 15:3761–74.
- Mi, H., T.J. Deerinck, M. Jones, M.H. Ellisman, and T.L. Schwarz. (1996) Inwardly rectifying K⁺ channels that may participate in K⁺ buffering are localized in microvilli of Schwann cells. *J Neurosci.* 16:2421–9.
- Mi, H., R.M. Harris-Warrick, T.J. Deerinck, I. Inman, M.H. Ellisman, and T.L. Schwarz. (1999) Identification and localization of Ca(2⁺)-activated K⁺ channels in rat sciatic nerve. *Glia.* 26:166–75.
- Moor, H. (1987) Theory and practice of high pressure freezing. In *Cryotechniques in Biological Electron Microscopy*. R.A.Z. Steinbrecht, K., editor. Springer-Verlag, Berlin. 175–191.
- Murray, N., and A.J. Steck. (1984) Impulse conduction regulates myelin basic protein phosphorylation in rat optic nerve. *J Neurochem.* 43:243–8.
- Nakamura, T., J. Blechman, S. Tada, T. Rozovskaia, T. Itoyama, F. Bullrich, A. Mazo, C.M. Croce, B. Geiger, and E. Canaani. (2000) huASH1 protein, a putative transcription factor encoded by a human homologue of the *Drosophila ash1* gene, localizes to both nuclei and cell-cell tight junctions. *Proc Natl Acad Sci U S A.* 97:7284–9.
- Nicastro, D., A.S. Frangakis, D. Typke, and W. Baumeister. (2000) Cryo-electron tomography of neurospora mitochondria. *J Struct Biol.* 129:48–56.
- Paul, D.L. (1995) New functions for gap junctions. *Curr Opin Cell Biol.* 7:665–72.
- Penczek, P., M. Marko, K. Buttle, and J. Frank. (1995) Double-tilt electron tomography. *Ultramicrosc.* 60:393–410.
- Perkins, G., C. Renken, M.E. Martone, S.J. Young, M. Ellisman, and T. Frey. (1997a) Electron tomography of neuronal mitochondria: three-dimensional structure and organization of cristae and membrane contacts. *J Struct Biol.* 119:260–72.
- Perkins, G.A., C.W. Renken, J.Y. Song, T.G. Frey, S.J. Young, S. Lamont, M.E. Martone, S. Lindsey, and M.H. Ellisman. (1997b) Electron tomography of large, multicomponent biological structures. *J Struct Biol.* 120:219–27.
- Poliak, S., L. Gollan, D. Salomon, E.O. Berglund, R. Ohara, B. Ranscht, and E. Peles. (2001) Localization of Caspr2 in myelinated nerves depends on axon-glia interactions and the generation of barriers along the axon. *J Neurosci.* 21:7568–75.
- Rios, J.C., M. Rubin, M. St Martin, R.T. Downey, S. Einheber, J. Rosenbluth, S.R. Levinson, M. Bhat,

- and J.L. Salzer. (2003) Paranodal interactions regulate expression of sodium channel subtypes and provide a diffusion barrier for the node of Ranvier. *J Neurosci.* 23:7001–11.
- Ritchie, J.M., and R.B. Rogart. (1976) The binding of labelled saxitoxin to normal and denervated muscle [proceedings]. *J Physiol.* 263:129P–130P.
- Ritchie, J.M., and R.B. Rogart. (1977) Density of sodium channels in mammalian myelinated nerve fibers and nature of the axonal membrane under the myelin sheath. *Proc Natl Acad Sci U S A.* 74:211–5.
- Rosenbluth, J. (1976) Intramembranous particle distribution at the node of Ranvier and adjacent axolemma in myelinated axons of the frog brain. *J Neurocytol.* 5:731–45.
- Salzer, J.L. (2003) Polarized domains of myelinated axons. *Neuron.* 40:297–318.
- Scherer, S.S., L.J. Bone, S.M. Deschênes, A. Abel, R.J. Balice-Gordon, and K.H. Fischbeck. (1999) The role of the gap junction protein connexin32 in the pathogenesis of X-linked Charcot-Marie-Tooth disease. *Novartis Foundation Symposium.* 219:175–187.
- Scherer, S.S., T. Xu, P. Crino, E.J. Arroyo, and D.H. Gutmann. (2001) Ezrin, radixin, and moesin are components of Schwann cell microvilli. *J Neurosci Res.* 65:150–64.
- Scherer, S.S., Y.T. Xu, P.G. Bannerman, D.L. Sherman, and P.J. Brophy. (1995) Periaxin expression in myelinating Schwann cells: modulation by axon-glial interactions and polarized localization during development. *Development.* 121:4265–73.
- Schnapp, B., and E. Mugnaini. (1975) The myelin sheath. Electron microscopic studies with thin section & freeze-fracture. In Golgi Centennial Symposium Proceedings. Raven Press, Inc., New York. 209–230.
- Shimoni, E., and M. Muller. (1998) On optimizing high-pressure freezing: from heat transfer theory to a new micro biopsy device. *J Microsc.* 192:236–47.
- Shoop, R.D., E. Esquenazi, N. Yamada, M.H. Ellisman, and D.K. Berg. (2002) Ultrastructure of a somatic spine mat for nicotinic signaling in neurons. *J Neurosci.* 22:748–56.
- Shrager, P. (1989) Sodium channels in single demyelinated mammalian axons. *Brain Res.* 483:149–54.
- Sima, A.A. (1993) Diabetic neuropathy—the presence and future of a common but silent disorder. *Mod Pathol.* 6:399–401.
- Soto, G.E., S.J. Young, M.E. Martone, T.J. Deerinck, S. Lamont, B.O. Carragher, K. Hama, and M.H. Ellisman. (1994) Serial section electron tomography: a method for three-dimensional reconstruction of large structures. *Neuroimage.* 1:230–43.
- Stiles, J.R., and T.M. Bartol. (2001) Monte Carlo methods for simulating realistic synaptic microphysiology using MCell. In Computational Neuroscience: Realistic Modeling for Experimentalists. E. De Schutter, editor. CRC Press.
- Stiles, J.R., T.M. Bartol, M.M. Salpeter, E.E. Salpeter, and T.J. Sejnowski. (2001) Synaptic variability: new insights from reconstructions and Monte Carlo simulations with MCell. In Synapses. W.M. Cowan, T.C. Sudhof, and C.F. Stevens, editors. Johns Hopkins University Press.
- Sward, C., C.H. Berthold, I. Nilsson-Remahl, and M. Rydmark. (1995) Axonal constriction at Ranvier's node increases during development. *Neurosci Lett.* 190:159–62.
- Tait, S., F. Gunn-Moore, J.M. Collinson, J. Huang, C. Lubetzki, L. Pedraza, D.L. Sherman, D.R. Colman, and P.J. Brophy. (2000) An oligodendrocyte cell adhesion molecule at the site of assembly of the paranodal axo-glial junction. *J Cell Biol.* 150:657–66.
- Trapp, B.D., S.B. Andrews, A. Wong, M. O'Connell, and J.W. Griffin. (1989) Co-localization of the myelin-associated glycoprotein and the microfilament components, F-actin and spectrin, in Schwann cells of myelinated nerve fibres. *J Neurocytol.* 18:47–60.
- Tsukita, S., M. Furuse, and M. Itoh. (1999) Structural and signalling molecules come together at tight junctions. *Curr Opin Cell Biol.* 11:628–33.
- Vabnick, I., S.D. Novakovic, S.R. Levinson, M. Schachner, and P. Shrager. (1996) The clustering of axonal sodium channels during development of the peripheral nervous system. *J Neurosci.* 16:4914–22.
- Vabnick, I., and P. Shrager. (1998) Ion channel redistribution and function during development of the myelinated axon. *J Neurobiol.* 37:80–96.
- Venken, K., J. Meuleman, J. Irobi, C. Ceuterick, R. Martini, P. De Jonghe, and V. Timmerman. (2001) Caspr1/Paranodin/Neurexin IV is most likely not a common disease-causing gene for inherited peripheral neuropathies. *Neuroreport.* 12:2609–14.
- Waxman, S.G., J.A. Black, P.K. Stys, and B.R. Ransom. (1992) Ultrastructural concomitants of

- anoxic injury and early post-anoxic recovery in rat optic nerve. *Brain Res.* 574:105–19.
- Waxman, S.G., and J.M. Ritchie. (1993) Molecular dissection of the myelinated axon. *Ann Neurol.* 33:121–36.
- Webster, H.D. (1971) The geometry of peripheral myelin sheaths during their formation and growth in rat sciatic nerves. *J Cell Biol.* 48:348–67.
- Webster, H.D., R. Martin, and M.F. O'Connell. (1973) The relationships between interphase Schwann cells and axons before myelination: a quantitative electron microscopic study. *Dev Biol.* 32:401–16.
- Wiley, C.A., and M.H. Ellisman. (1980) Rows of dimeric-particles within the axolemma and juxtaposed particles within glia, incorporated into a new model for the paranodal glial-axonal junction at the node of Ranvier. *J Cell Biol.* 84:261–80.
- Wiley-Livingston, C., and M.H. Ellisman. (1980) Development of axonal membrane specializations defines nodes of Ranvier and precedes Schwann cell myelin elaboration. *Dev Biol.* 79:334–55.
- Wiley-Livingston, C.A., and M.H. Ellisman. (1981) Myelination-dependent axonal membrane specializations demonstrated in insufficiently myelinated nerves of the dystrophic mouse. *Brain Res.* 224:55–67.
- Wood, J.G., D.H. Jean, J.N. Whitaker, B.J. McLaughlin, and R.W. Albers. (1977) Immunocytochemical localization of the sodium, potassium activated ATPase in knifefish brain. *J Neurocytol.* 6:571–81.
- Wurtz, C.C., and M.H. Ellisman. (1986) Alterations in the ultrastructure of peripheral nodes of Ranvier associated with repetitive action potential propagation. *J Neurosci.* 6:3133–43.
- Yamamoto, K., A.C. Merry, and A.A. Sima. (1996) An orderly development of paranodal axoglial junctions and bracelets of Nageotte in the rat sural nerve. *Brain Res Dev Brain Res.* 96:36–45.